DOE/ER/4504--T1

Final Report

A Robust Economic Technique for Crosswell Seismic Profiling

Grant No. DE-FG03-95ER14504

Prepared for the Basic Energy Science Division
of the U.S. Department of Energy

by

Bureau of Economic Geology
Noel Tyler, Director
The University of Texas at Austin
Austin, Texas 78713-8924

Principal Investigators: Bob A. Hardage
James L. Simmons, Jr.

January 1998

DISCLAIMER

DISCLAIMER

Portions of this document may be illegible electronic image products. Images are produced from the best available original document.

Executive Summary

This report is the final report describing work done under research project DE-FG03-95ER14504, titled, *A Robust Economic Technique for Crosswell Seismic Profiling*, which was funded by the U.S. Department of Energy.

The objective of this research program was to investigate a novel way to acquire crosswell tomographic data, that being to use a standard surface-positioned seismic energy source stationed inline with two wells that have downhole receiver arrays. This field technique differs from the traditional way that crosswell tomography is done, which requires that a downhole receiver array be in one well and that a downhole seismic source be in a second well.

Several potential advantages can result by using a surface-based source rather than a downhole source to acquire crosswell tomographic data. Included in these advantages would be: (1) surface-based seismic sources emit more energy than do downhole seismic sources, thus receiver wells can be spaced at greater distances, (2) surface-based sources are more reliable than downhole sources and are more accessible if field repairs have to be done, and (3) downhole receivers can be deployed in a wider range of well conditions (cased hole, open hole, tubing, high-pressure lubricators, etc.) than can downhole sources, allowing crosswell tomography to be done in a wider variety of reservoirs.

However, several potential shortcomings may occur if a surface-based source is used to acquire crosswell tomographic data. The principal concerns are: (1) source-to-receiver raypaths may not traverse the interwell space in a way that allows a robust tomographic inversion to be done, (2) errors in measuring arrival times may be too large for traveltime inversion to be stable, and (3) the reduced bandwidths generated by surface-based sources may not allow some interwell targets to be detected.

The purpose of the research effort was to evaluate the relative merits of these potential advantages and pitfalls of surface-source crosswell tomography, which some also refer to as twin-receiver-well crosswell tomography. The principal findings were: (1) surface-source crosswell tomography is a viable technology and can be used in appropriate reservoir conditions, (2) raypath modeling should be done to determine if the targeted interwell space is properly illuminated by surface-generated wavefields before proceeding to collect surface-source tomographic data, (3) crosswell data generated by a surface-based source are subject to a greater range of traveltime errors than are data generated by a downhole source, primarily due to shot statics caused by variable weathered layers, and (4) the accuracy and reliability of the interwell tomogram increase

as more independent velocity information (sonic logs, velocity checkshots, vertical seismic profiles, downhole-source crosswell data) is available to constrain the inversion.

The surface-source approach to crosswell tomography was evaluated by recording twin-receiver well data at the Texaco Borehole Test Site in Humble, Texas. (end) hanging hydrophone arrays deployed in two separate wells were used for th receiver arrays, and four truck-mounted Bolt airgun units positioned inline with these two receiver wells and at four separate offset distances were used for the surface-based sources. This report presents these surface-source crosswell data and the crosswell tomograms that they generated.

The format of this report is structured like that used for the geological circulars issued by the Bureau of Economic Geology at The University of Texas at Austin. The Bureau infuses approximately 40,000 publications into the public sector each year, and the research findings amassed in this DOE-funded program will be publicly circulated as an official Bureau publication. A shorter version of this final report is being submitted to the journal *Geophysics* for peer review and international exposure.

Summary of Field Data Tests

Crosswell seismic tomography attempts to image the interwell velocity field using traveltimes of transmitted waves generated by a downhole source and recorded by downhole receivers. Traveltimes of the transmitted waves are governed by the subsurface velocities along their travelpaths. This sensitivity provides the basis for adjusting an initial velocity model such that the traveltimes predicted by raytracing best match the observed traveltimes.

Twin- vertical-seismic-profile simulation of crosswell (TVSC) tomography uses the first-arrival times from wavefields generated by number of surface sources positioned in-line with two receiver wells. The differential traveltimes between the receiver wells are used to estimate the interwell velocities. As a result, TVSC tomography is theoretically independent of the subsurface velocities outside of the interwell space even though the VSP wavefields traveled through these portions of the subsurface.

TVSC tomography is evaluated on synthetic and real data. The velocity model is parameterized with cubic B-splines, and adjustments to the initial velocity model are obtained using a least-squares solution. A model covariance matrix designed to minimize variations in the spatial derivatives of the velocity updates is incorporated into the inverse problem.

The synthetic examples have differential traveltimes between the receiver wells on the order of 70-80 ms. Velocities can be recovered from noise-free data with local errors as large as 2 percent and an associated data misfit of +/- 1 ms. Use of the model covariance matrix illustrates the tradeoff between data fit and model reasonableness. Examples with Gaussian random noise as large as +/- 6 ms added to the differential traveltimes show local velocity errors as large as 5 percent, with 95 percent of the data predicted to within +/- 5 ms.

Field data were acquired at Texaco's Borehole Test Site located near Humble, Texas. Wavefields from four offset surface-source locations were recorded by six-element hydrophone arrays (10 ft receiver spacing, 50 ft maximum recording aperture) in two receiver wells over the depth interval from 2550 to 1540 ft. Three-component geophone data recorded in a third well over the depth interval from 1500 to 50 ft provide information on the common shot statics (+/- 3 ms) and overall shot reproducibility.

VSP data quality is quite variable. Overall signal-to-noise ratio varies from 15.5 to 4.8 decibels (root-mean-square amplitude). The differential traveltimes (between receiver wells) are roughly 50-60 ms. Noise in the first-arrival times produced by tube waves and timing inconsistencies that occurred in the data acquisition is on the order of +/- 5 ms.

TVSC tomography predicts the measured first-arrival times to within +/- 5 ms. Inversion results obtained low and high noise levels in the data illustrates the tradeoff between data fit and model reasonableness.The resulting velocity estimate indicates an overall increase in velocity from 6800 ft/s at 1540 ft depth to 7600 ft/s at 2550 ft depth, with a sharp increase at 2100 ft depth.

Surface-source to downhole-receiver traveltime inversion reproduces the data to within +/- **3 ms** and is less sensitive to noise than the TVSC inversion. Velocity models estimated by the TVSC and surface tomography inversions are similar.

Introduction

A conventional crosswell seismic experiment is conducted with downhole seismic sources in one well, and receivers (hydrophones and/or geophones) in the receiver well. The seismic source is fired at a number of depths and the receivers record the seismic wavefield generated by each shot. The seismic wavefields include a variety of compressional and shear wave modes: direct waves, head waves, reflections, converted waves, and tube waves. From this data, the potential exists to image the interwell space.

One application of crosswell seismic data is crosswell seismic tomography. Tomography attempts to reconstruct an image from sums (integrals) of projections that have passed through the image (Dines and Lytle, 1979; Herman, 1980; Coulam et al., 1981). Crosswell seismic tomography attempts to construct an image of the interwell velocity model that predicts the measured compressional-wave (P-wave) first-arrival times. These first arrivals propagate directly from source to receiver. Given an adequate angular aperture of raypath coverage, the interwell velocity model can be reconstructed using approaches similar to those used in medical imaging applications. The inverse problem involves the solution of a set of simultaneous linear equations. Adjustments to the initial velocity model are found that result in computed first-arrival times (by raytracing) that best predict the observed first-arrival times (Bois et al., 1972; Wong et al., 1983; Peterson et al., 1985; Gustavsson et al., 1986; Ivansson, 1986; McMechan, 1988; Bregman et al., 1989a; Lines and LaFehr, 1989).

Crosswell tomography was originally advertised as being the seismic method that could provide the highest resolution of the interwell space. Seismic wavelengths are much smaller in crosswell data (higher frequencies, shorter travel paths) than in surface

reflection data. In general, first-arrival time tomography has not provided the high resolution results that were anticipated. Traveltimes are inherently low frequency, and cell-based model parameterizations have often produced velocity models very different from available sonic logs. More recent work that attempts to image the interwell space from crosswell seismic reflections is promising (Harris et al., 1995; Lazaratos et al., 1995; Zhou et al., 1995).

Widespread application of crosswell seismic technology has been impeded by several limitations: small crosswell ranges, complex well-preparation logistics, and high data-acquisition costs (Blakeslee, 1994). In addition, the results obtained from crosswell data analysis have often not lived up to expectations or justified the cost.

Blakeslee et al. (1993) and Blakeslee (1994) propose a twin-VSP simulation of a crosswell (TVSC) seismic experiment. Surface seismic sources are located in-line with, and off-end to, two receiver wells. Wavefields are recorded in each of the two receiver wells from a number of surface source locations. First-arrival times from the VSP wavefields are then used to estimate the interwell velocities using inversion techniques similar to those used in standard crosswell tomography.

There are several potential benefits to the TVSC approach. Larger energy sources may be used which allow larger interwell separations to be imaged. Since the differential traveltimes between the two receiver wells are used to infer the interwell velocity model, knowledge of the velocities outside of the interwell space is not required. Blakeslee et al. (1993) and Blakeslee (1994) also propose cost reduction as a major potential benefit.

The TVSC tomography approach is presented and evaluated on synthetic and real data. Two-dimensional cubic B-splines (Inoue, 1986) describe the interwell velocity model. The model parameterization and associated raytracing are cast into a least-squares inversion.

Field data recorded at Texaco's Humble Test Site are available for analysis. Wavefields from four offset surface-source locations were recorded by hydrophones in two receiver wells. Wavefields were also recorded in a third well containing cemented-in-place, 3-component geophones. These geophone data provide quality control for the experiment. Some of the first-arrival time data cannot be used in the inversion because of the data acquisition geometry. In addition, the overall data quality is quite variable. Nevertheless, the TVSC inversion is adapted and applied to the real data, as is more conventional surface-source to downhole-receiver tomography.

The TVSC Approach

Twin-VSP simulation of crosswell tomography (TVSC) was proposed by Blakeslee et al. (1993) and Blakeslee (1994). Assume a 2-D VSP recording geometry with two receiver wells and a number of surface seismic sources positioned in-line with, and on either side of, the receiver wells. VSP wavefields from each of the source locations are recorded in each receiver well (Figure 1). The premise of the TVSC approach is that the interwell velocity model can be estimated from the measured first-arrival times of the VSP wavefields *without* regard to the velocity model that lies *outside* of the interwell space. It also follows that knowledge of the absolute surface-source receiver-well offsets is not needed.

For a given source, the traveltimes recorded in the near receiver well are referred to as the reference times and are considered to be secondary sources (Figures 1b and 1c). Traveltimes recorded in the far receiver well are the data to be reproduced and referred to as the observed traveltimes. The TVSC algorithm attempts to match the observed traveltimes given the reference (secondary source) traveltimes and an estimate of the interwell traveltimes. The observed traveltimes are estimated as the sum of the reference and interwell traveltimes. Note that the reference traveltimes are fixed and are influenced by velocities outside of the interwell region. Meanwhile the interwell traveltime (and raypath) depend only upon the interwell velocity model.

For a particular receiver in the far receiver well, the traveltime and raypath to each of the near-well receivers are determined by raytracing (Figure 1d). This produces a vector of differential traveltimes. The differential traveltimes are added to the reference traveltimes. Fermat's principle is invoked by selecting the minimum traveltime, which also provides the associated raypath, between the receiver wells (Figure 1e).

The process is repeated for all receivers in the far well. Traveltimes and raypaths from each receiver depth to all receivers in the near well are calculated. Each vector of differential traveltimes is added to the reference times. The minimum traveltime of each sum gives an estimate of the first-arrival time from the surface source to the particular far-well receiver.

The goal of TVSC tomography is to estimate the interwell velocity model given the reference and observed first-arrival times, thereby simulating a crosswell traveltime tomography experiment. The minimum traveltime estimates are the predicted traveltimes. The interwell velocity model is then modified such that the predicted first-arrival times best agree with the observed first-arrival times. Note than an updated velocity model affects only the differential traveltimes, their associated raypaths, the resulting sum of the

reference and differential traveltimes and, thus, the predicted first-arrival time from the surface source to the observation well.

A least-squares solution is used to iteratively adjust the initial velocity model. Cubic B-splines (Inoue, 1986) describe the interval velocity model, and raytracing calculates the first-arrival times predicted by the current velocity model. A priori information concerning the variances and covariances of the model parameters, and noise in the data are incorporated into the inverse problem.

The General Inverse Problem: Maximum-likelihood approach

The general problem of estimating a velocity model from traveltime data is inherently nonlinear since the raypaths and the traveltimes depend on the velocity model. A variety of linear and nonlinear approaches are available for updating the interwell velocity model in an automated fashion. Although this problem is nonlinear, we reach a solution by solving a sequence of linearized approximations. A linearized inverse problem relates the model parameter updates to the data misfit (difference between the observed data and the predicted data) with the Frechet derivatives. Frechet derivatives are partial derivatives that indicate how the data are expected to change due to a perturbation in each of the model parameters.

In general, nonlinear forward modeling relates the model parameters **m** to the data **d** as

$$\mathbf{d} = g(\mathbf{m}), \tag{1}$$

where g is the nonlinear forward modeling operator. Vectors are noted in bold face and matrices are noted in bold with an underscore as **d** and $\underline{\mathbf{G}}$, respectively. The maximum-likelihood approach of Tarantola (1987) assumes that the probability density functions describing the a priori data errors, model parameter uncertainties, and errors in the forward modeling are Gaussian. The a posteriori probability density function for the model parameters is also Gaussian, and is maximized when S(**m**) is minimized. The quadratic objective function S(**m**) is defined as

$$S(\mathbf{m}) = \frac{1}{2}\left[(\mathbf{d}_{obs} - g(\mathbf{m}))^T \underline{\mathbf{C}}_d^{-1}(\mathbf{d}_{obs} - g(\mathbf{m})) + (\mathbf{m} - \mathbf{m}_{prior})^T \underline{\mathbf{C}}_m^{-1}(\mathbf{m} - \mathbf{m}_{prior})\right]. \tag{2}$$

where T is the transpose operator, the observed data are $\mathbf{d}_{obs}$, and the initial model parameters are contained in $\mathbf{m}_{prior}$. The inverse data covariance, $\underline{\mathbf{C}}_d^{-1}$, describes the noise in

the data while the inverse model covariance, $\underline{\mathbf{C}}_m^{-1}$, describes the uncertainties in the a priori model. S(**m**) is simply a scalar for the current model parameters **m**.

The forward modeling is linearized around the initial model, $\mathbf{m}_{prior}$, as

$$g(\mathbf{m}) \approx g(\mathbf{m}_{prior}) + \underline{\mathbf{G}}(\mathbf{m} - \mathbf{m}_{prior}), \tag{3}$$

where $\underline{\mathbf{G}}$ represents the Frechet derivative operator evaluated at $\mathbf{m}_{prior}$.

The maximum-likelihood solution to equation (2) is

$$\mathbf{m}_{new} = \mathbf{m}_{old} + \left[\underline{\mathbf{G}}^T\underline{\mathbf{C}}_d^{-1}\underline{\mathbf{G}} + \underline{\mathbf{C}}_m^{-1}\right]^{-1}\left[\underline{\mathbf{G}}^T\underline{\mathbf{C}}_d^{-1}\Delta\mathbf{d} + \underline{\mathbf{C}}_m^{-1}\left(\mathbf{m}_{prior} - \mathbf{m}_{old}\right)\right], \tag{4}$$

where $\Delta\mathbf{d}$ is the data misfit defined as $\Delta\mathbf{d} = \mathbf{d}_{obs} - g(\mathbf{m}_{old})$, and the parameters of the previous model are contained in $\mathbf{m}_{old}$. Note that for the first iteration, $\mathbf{m}_{old} = \mathbf{m}_{prior}$.

Minimization of the data misfit alone forces the predictions to match the observations. As is often the case in geophysical inversion, the observations may be accurately reproduced but the resulting model estimate is often unreasonable. Incorporation of the model covariance matrix $\underline{\mathbf{C}}_m^{-1}$ helps to keep the estimated model close to the a priori model and can be used to impose smoothness into the model parameter updates. The degree to which the data can be reproduced with a reasonable model depends on the appropriateness of the model parameterization, the model and data covariance matrices, and the forward modeling algorithm.

Model Parameterization

Cubic B-splines provide a parameterization well suited for first-arrival time inversion. B-splines are smooth, continuous mathematical functions. With this parameterization, the near-surface velocity field can be described with relatively few parameters. Cubic B-splines (Inoue,1986) describe the interval velocity, as a function of horizontal position and depth, as a weighted sum of cubic polynomial basis functions. The earth model is parameterized with NX by NZ equally-spaced grid nodes. The B-spline representation of the velocity model is

$$V(z,x) = \sum_{j=1}^{NZ+3}\sum_{i=1}^{NX+3} c_{ij}F_i(x)E_j(z), \tag{5}$$

where V(z,x) is the interval velocity as a function of depth z, and lateral position x. The product of one-dimensional B-spline basis functions $F_i(x)$ and $E_j(z)$ results in a Gaussian-like two-dimensional basis function (Figure 2a). B-spline coefficients c_{ij} are the amplitudes of the basis functions, and have the same units as the function being fit (in this case velocity). V(z,x) is represented as a weighted linear combination of Gaussian-like basis functions.

The basis functions overlap and are not independent. Figure 2b shows a profile through V(z,x) taken at a fixed x which lies at a grid node. A continuous V(z) is represented with overlapping basis functions (dashed curves). At any point in the z-x domain, 16 non-zero basis functions (in two dimensions) interact to give the value of the function V(z,x) at that point.

Forward Modeling: Raytracing

The traveltime of a ray is simply the integral along the raypath of the reciprocal of the velocity as

$$T = \int_{ray} \frac{ds}{V(z,x)}, \tag{6}$$

where ds is the arclength, and V(z,x) represents the velocity along the raypath trajectory. Raypaths follow the well-known principle of minimum traveltime and their behavior is governed by the raytracing equations. Different approaches to raytracing can be employed depending on the particular parameterization of the velocity model. Since the velocity model varies smoothly as a function of (z,x), simple integration of the ray-tracing equations produces the raypath trajectories and the first-arrival times (Cerveny and Hron, 1980).

Frechet Derivatives

Frechet derivatives represent the partial derivatives of the data with respect to the model parameters. A change in velocity produces a change in the traveltime of a ray due to the perturbed velocity and the modified raypath. Backus and Gilbert (1969) show that to first order, the effect on the traveltime of a given velocity perturbation can be approximated by the effect of propagation through the perturbed velocity field along the

unperturbed raypath. This means that the derivative of the traveltime with respect to a velocity perturbation can be evaluated along the raypath through the reference (unperturbed) model.

Frechet derivatives are the expected change in the first-arrival time for a particular ray produced by a perturbation in a B-spline coefficient. Let T_k represent the first-arrival time for a particular source-receiver pair . The Frechet derivatives are expressed as

$$G_{kn} = \frac{\partial T_k}{\partial c_{ij}} = \int_{ray} \frac{\partial T_k}{\partial V} \frac{\partial V}{\partial c_{ij}}, \tag{7}$$

where G_{kn} denotes the row of $\underline{G}$ corresponding to data point k, and the column of $\underline{G}$ corresponding to model parameter n, where n=1... (NX+3)*(NZ+3). The velocity, V, is assumed to be a function of position within the z-x domain as V(z,x).

Using equations (5) and (7),

$$G_{kn} = \frac{\partial T_k}{\partial c_{ij}} = \int_{ray} \frac{-ds}{V^2} F_i(x) E_j(z). \tag{8}$$

The derivative of the velocity field with respect to a B-spline coefficient is simply equal to the basis functions that multiply that coefficient. Computationally, the integral in equation (8) is approximated as a discrete sum along the nodes of each raypath. The Frechet derivatives are computed simultaneously as the rays are traced through the current velocity model. This approach is similar to that employed by Bishop et al. (1985).

Model Covariance

The inverse model covariance matrix $\underline{C}_m^{-1}$ is interpreted directly as a smoothing operator that has non-zero off-diagonal terms. As a result, smoothing is introduced and control on the interaction between B-spline coefficients is imposed. $\underline{C}_m^{-1}$ is designed to

minimize a weighted combination of the spatial derivatives of the velocity field. The inverse model covariance matrix is defined as

$$C_m^{-1} = \lambda_1 \frac{\partial V(z,x)}{\partial x} + \lambda_2 \frac{\partial V(z,x)}{\partial z} + \lambda_3 \frac{\partial^2 V(z,x)}{\partial x^2} + \lambda_4 \frac{\partial^2 V(z,x)}{\partial z^2}. \qquad (9)$$

The partial derivatives in equation (9) are determined analytically. Each component is a two-dimensional matrix with dimensions number of model parameters by number of model parameters. Weighting coefficients, λ, determine how much each term contributes to $\underline{C}_m^{-1}$. Nonzero λ imposes smoothing to the model parameter updates. This form of $\underline{C}_m^{-1}$ limits variations in the corresponding spatial derivatives of the model parameter updates. For example, to limit variations in the curvature (second derivative) of the velocity updates in the x- and z-directions, one would set λ_3 and λ_4 to be nonzero.

Data covariance

Noise in the data is assumed to be uniform and independent. In general, the data covariance matrix is defined simply as

$$\underline{C}_d = \sigma_d^2 \underline{I}, \qquad (10)$$

where σ_d^2 is the variance of the noise, and $\underline{I}$ is the identity matrix.

The maximum-likelihood solution of equation (4) is modified so that the solution to the inverse problem becomes

$$\mathbf{m}_{new} = \mathbf{m}_{old} + \left[\underline{G}^T\underline{G} + \sigma_d^2\underline{C}_m^{-1}\right]^{-1}\underline{G}^T\Delta\mathbf{d}. \qquad (11)$$

The weighting coefficients λ impose the desired smoothness into $\underline{C}_m^{-1}$. This approach to $\underline{C}_m^{-1}$ also constrains those model parameters which are poorly determined by the data (Squires and Cambois, 1992). σ_d^2 is simply a scalar that roughly accounts for the noise in the data and weights the importance of the inverse model covariance matrix relative to $\underline{G}^T\underline{G}$.

This least-squares solution provides updates to the current model parameters. The true maximum-likelihood solution (equation (4)) keeps the current model close to the initial model through the $\underline{C}_m^{-1}\left(\mathbf{m}_{prior} - \mathbf{m}_{old}\right)$ term. The least-squares solution of equation (11) attempts to keep the current model close to the initial model through σ_d^2, $\underline{C}_m^{-1}$, and the B-spline model parameterization. The relatively low frequency B-spline model parameterization is less sensitive to noise than the more common cell parameterizations.

Note that if only a subset of raypaths are used in the inversion, the magnitude of the elements of $\underline{\mathbf{G}}^T\underline{\mathbf{G}}$ will be smaller than if all rays are included. In order to maintain the same relative importance of $\underline{\mathbf{C}}_m^{-1}$ on the inversion, the magnitude of σ_d^2 must be modified appropriately.

Synthetic Examples: Noise-Free Data

The TVSC approach is evaluated on several synthetic examples. Synthetics serve to demonstrate the algorithm and to evaluate the model parameterization and inversion parameters selected.

The velocity model used to generate the first-arrival times is shown in Figure 3a. Two receiver wells are indicated and span a depth range of 20-1000 ft with a 20 ft depth spacing. Traveltimes from four surface-source locations are measured at each receiver well. An enlarged view of the true and initial velocity models is shown in Figure 3b. The initial velocity model is laterally invariant and consists of a continuous velocity increase with depth. All of the synthetic examples have the same initial velocity model.

First-arrival times from the surface sources to each of the downhole receivers are shown in Figure 3c. The velocity gradient causes the first-arrivals from Source A to Well 1, Source A to Well 2, and Source B to Well 1 to arrive earlier at the deeper receivers than at shallower depths. From these eight traveltime curves, the TVSC algorithm uses four curves as the reference times (A-1, B-1, C-2, D-2) and four curves as the observations to be reproduced (A-2, B-2, C-1, D-1).

The interwell velocity model is parameterized with 20 B-splines in the x-dimension spaced 35 ft apart, and 25 B-splines in the z-dimension spaced 48 ft apart. There are 500 model parameters to be estimated in the inversion. The initial model parameters $\mathbf{m}_{\mathbf{prior}}$ are the B-spline coefficients, c_{ij}, that describe the initial velocity model.

Contributions to $\underline{\mathbf{G}}^T\underline{\mathbf{G}}$ and $\underline{\mathbf{G}}^T\Delta\mathbf{d}$ (from equation 11) are calculated concurrently as each ray is traced. Since there are 500 model parameters, $\underline{\mathbf{G}}^T\underline{\mathbf{G}}$ is 500 by 500 in size, as is $\underline{\mathbf{C}}_m^{-1}$. Organization of $\underline{\mathbf{G}}^T\underline{\mathbf{G}}$ is dependent on the ordering of the model parameters in the columns of $\underline{\mathbf{G}}$ and consequently in the rows of $\Delta\mathbf{m}$. The relative magnitudes of the elements of $\underline{\mathbf{G}}^T\underline{\mathbf{G}}$ are determined by the raypath coverage.

Inversion results showing the velocity estimates, error in the velocity estimates, and the data misfit are shown in Figures 4-6, respectively. The specific examples show the effects that $\underline{\mathbf{C}}_m^{-1}$ and noise in the data have on the inversion results. Each inversion is performed for five iterations. After each iteration, the model parameter updates are added

to the prior model parameters (equation 11). The updated model is then used to calculate the updated data misfit $\Delta\mathbf{d}$, $\underline{\mathbf{G}}^T\underline{\mathbf{G}}$, and $\underline{\mathbf{G}}^T\Delta\mathbf{d}$.

Estimated velocity models are shown in Figures 4a, 4b, and 4c, and Figures 5a, 5b, and 5c show the error between the true and estimated velocity models. Velocity estimates after each of five iterations are shown along with the true velocity model. The initial data misfit (difference between true first-arrival times and the times predicted by the initial velocity model) as well as the final data misfit (after five iterations) are shown in Figure 6. Four misfit values at each receiver depth correspond to the four sets of predicted traveltimes. The influence of the inverse model covariance matrix increases from Figure 6a to 6b to 6c.

Figures 4a, 5a, and 6a show the results obtained using diagonal damping of $\underline{\mathbf{G}}^T\underline{\mathbf{G}}$ ($\underline{\mathbf{C}}_m^{-1}=\mathbf{I}$). Presence of the dipping high velocity region causes the initial misfit to increase with depth. The final data misfit is on the order of +/- 0.5 ms, and has a relatively constant magnitude with increasing receiver depth (Figure 6a).

The basic form of the true velocity model is estimated after one iteration (Figure 4a). The dipping interface of the high velocity region is apparent. Velocities in the deeper portion of the interwell space are modified in later iterations. Note the diagonal streaking (upper right to lower left) in the 300-600 ft depth range, which is especially obvious in Figure 5a. This streaking is an artifact and is not present in the true velocity model. Also note that velocities deeper than the deepest receivers are not modified from their initial values.

Inversion results obtained using the full inverse model covariance matrix are shown in Figures 4b, 5b, and 6b. $\underline{\mathbf{C}}_m^{-1}$ now has nonzero off-diagonal terms and has the form of equation (9). Smoother velocity estimates are obtained and the diagonal streaking noted in the previous example is reduced (Figure 5b). The dominant term in $\underline{\mathbf{C}}_m^{-1}$ is $\lambda_4 \frac{\partial}{\partial z^2}$. As a result, variations in the curvature of the velocity estimates (in depth) are reduced. This effect is seen most clearly at depths below the deepest receivers which have changed from their initial values in order to minimize variations in the curvature with depth.

The observations are again predicted to within +/- 0.5 ms (Figure 6b). The degree of fit to the data has not been appreciably degraded by use of $\underline{\mathbf{C}}_m^{-1}$, and the estimated velocity model better resembles the true velocity model. In effect, the unconstrained solution in Figure 6a attempts to account for the approximations involved in the raytracing and results in a slightly smaller data misfit (Figure 4a), at the expense of a more erroneous velocity estimate.

Results where the importance of $\underline{\mathbf{C}}_m^{-1}$ is increased by increasing σ_d^2 are shown in Figures 4c, 5c, and 6c. The velocity estimates are even smoother than in Figures 4b and

5b, and the data misfit is noticeably larger (Figure 6c). This issue of model smoothness and reasonableness versus degree of data misfit is fundamental in all types of tomographic inversions.

Synthetic Examples: Effect of Noise

The previous examples assumed noise-free first-arrival times. Results where Gaussian random noise is added to the first-arrival times are shown in Figures 4d-e, 5d-e, and 6d-e. A histogram of the noise is shown in Figure 6. The noise is added to the reference and observed first-arrival times. Also shown in Figure 6 is the initial data misfit in the presence of the Gaussian noise.

Inversion results are shown using the same $\underline{\mathbf{C}}_m^{-1}$ as in the noise-free examples but for increased values of σ_d^2. A larger value for σ_d^2 is used in example e than in example d. Beyond the first iteration, the higher spatial frequency components of the velocity estimates are modified. The dipping region is recognized but is located at deeper depths than in the true model. Apparent lateral velocity variations are introduced due to the noise in the data. The data misfit is generally within +/- 5 ms and is relatively uniform with depth (Figure 6d).

Results illustrating the effect of increasing the importance of $\underline{\mathbf{C}}_m^{-1}$ by increasing σ_d^2 are shown in Figures 4e, 5e, and 6e. The solution now accounts for the increased level of noise by keeping the model update closer to the initial model and weighting the model smoothness constraints more heavily. Smoother velocity estimates result, and the data misfit is very similar to that of Figure 4d. The dipping region is again recognized but misplaced in depth. The apparent lateral velocity variations are of lower spatial frequency than in Figure 6d because of the increased influence of $\underline{\mathbf{C}}_m^{-1}$.

As expected, the presence of noise in the traveltime data degrades the velocity estimates. The sharp velocity contrast is misplaced in depth and apparent lateral velocity variations are introduced.

Application of TVSC Approach to Real Data

Blakeslee et al. (1993) and Blakeslee (1994) demonstrate TVSC tomography only on synthetic noise-free data. Their examples also assume that the receiver wells are fully

instrumented, meaning that traveltimes are recorded in the receiver wells from a maximum depth to the ground surface.

The first application of TVSC tomography to real VSP data is presented. Real data results must be interpreted realizing that the real VSP data are not noise free, the true interwell velocity model is not known, and the receiver wells are not fully instrumented. Development of TVSC tomography based on a cubic B-spline representation of the velocity model was done with these factors in mind.

Field Test Site, Field Geometry, and Data Acquisition

The surface-source twin receiver-well field test was performed at Texaco's Borehole Geophysics Test Site near Humble, Texas. This test area is located within an active oil field. Vehicular traffic, pumping oil wells near the receiver wells, and well workover activity within 200 ft of the receiver wells all generated coherent noise in the recorded data. In addition, the air pressure disturbance produced by aircraft approaching Houston Intercontinental Airport generated tube waves in both receiver wells.

Wells 1 and 2 are the receiver wells, and four source locations are inline with the two receiver wells. The source positions (A, B, C, D) and the receiver wells are indicated on the aerial photograph (Figure 7). A nearby well that contains 30 three-component geophones cemented-in-place at depths of 50 ft - 1500 ft at a 50 ft depth increment is also marked. Data recorded in this well are used to provide shot-static corrections.

Bolt land air-guns served as the surface energy sources. A single air-gun vehicle was stationed at each of the four source locations. The sources at locations A, B, and C were 60-in^3 air guns and were positioned on gravel roads. Source D was located on soft ground and was a larger 75-in^3 air gun.

A six-level hydrophone array having elements spaced 10 ft apart was stationed in each of the receiver wells. The receivers were free hanging, which enabled rapid receiver movements but increased susceptibility to tube waves.

The total depth interval spanned by the downhole receivers is 1540-2550 ft. Given that the 6-element hydrophone strings span a 50-ft depth range, the hydrophone strings were positioned at 17 sequential depth stations in order to cover the 1010-ft aperture. Each 6-element hydrophone array records the wavefield from each source location producing the equivalent of common shot gathers. Shots at each source location were taken as the hydrophone arrays were moved sequentially uphole in 60 ft increments. As a

result, there is no data overlap between adjacent depth stations. The complete VSP's are comprised of traces recorded at the 102 individual depths.

At each of the four source locations (A, B, C, D), at least 17 shotpoint gathers were acquired; each of which contained 90 traces. Twelve traces are the hydrophone data in the receiver wells, and 78 traces are the 3-component geophone data from the nearby well. Vertical component data were recorded in the cemented geophone well only at depths from 650-1500 ft since the first 12 channels were used to record the hydrophone data.

At some receiver depths, multiple shots from the same surface location were acquired. This multiplicity of data at common receiver depths provides information on the overall reproducibility of the shots (similarity of the waveforms), and information regarding a component of the timing inconsistencies related to variations in the seismic origin time. Ideally, a *one-hydrophone overlap* (a 50 ft uphole move rather than a 60 ft uphole move) would have provided redundant information that would help to deduce the timing inconsistencies.

Field Seismic Data

Seismic data from source location A recorded in well 2 are shown in Figure 8 as common-shot gathers and as common-depth gathers. In general, the waveforms are relatively consistent at receiver depths of 2550, 2540, 2530, and 2520 ft. The largest variance in the waveforms occurs at depths of 2510 and 2500 ft near 620 ms, which happens to be the P-wave first arrival. The P-wave first arrival is apparent as the trough preceding the strong peak near 620 ms. Note the timing variations, however, of the first strong peak on all depth gathers.

Assume that the bulk static shift in the seismic origin-time, produced by the time delay from when the receivers begin recording to when the source is fired, from the land air-gun at a source location, $\Delta t^{bulk}_{location}$, is the same for all shots at that location. Timing variations seen in Figure 8 are then attributed to timing inconsistencies of individual shots, $\Delta t^{shot}_{location}$, and/or timing inconsistencies in the hydrophones, Δt^{rec}_{depth}, and/or additive noise, Δt_{noise}. The total timing uncertainty as a function of source location, shot, and receiver depth is defined as

$$\Delta T = \Delta t^{bulk}_{location} + \Delta t^{shot}_{location} + \Delta t^{rec}_{depth} + \Delta t_{noise}. \quad (12)$$

Radio relayed time-breaks were recorded for each individual shotpoint. Later analysis showed that these data were not reliable and consequently discarded.

Four of the full-fold VSP gathers are shown in Figures 9a, 9b, 9c, and 9d. Multiple traces at a given depth are stacked to produce a single trace at each depth from 2550-1540

ft, in 10 ft increments. Data recorded in well 1 have a much poorer signal-to-noise ratio than the data recorded in well 2. Source location D has by far the poorest signal-to-noise ratio. Apparent tube wave energy precedes the first arrival and has both normal and reverse moveout. In general, the P-wave first arrival can be identified. The actual timing of the P-wave first arrival needed for the traveltime inversion is more tenuous.

Vertical banding is clearly evident in Figure 9. Each band is 6-traces wide and corresponds to traces recorded from a particular shotpoint. Despite the drastic variations in signal-to-noise ratio and the traveltime variances, the traveltime of the P-wave first arrival is picked to the nearest time sample (1 ms).

The three-component cemented geophones are used as a reference to infer the magnitude of the $\Delta t^{shot}_{location}$ timing variations. Figure10 shows portions of the three-component geophone data (vertical =V, horizontal 1=H1, and horizontal 2=H2) acquired at depths of 800, 1100, and 1300 ft for all shots from the specified source location. Recall that there are 17 effective shotpoints for the 6-element hydrophone arrays over the 1010 ft depth interval of interest. An average first-arrival time is obtained for each geophone depth and geophone component from a particular source location as, $\bar{t}^{geophone}_{location}$.

Each panel shows a 50-ms time window around the first-arrival for each trace (the first strong peak). These data have been amplitude equalized for display. If the only component involved in the seismic time-origin question is $\Delta t^{bulk}_{location}$, then the data within each panel should have the same first-arrival time.

The arrival time information is displayed in Figure 11. Each vertical line shows the difference in the measured first-arrival time of a particular (shot-geophone-location) combination, $t^{shot,geophone}_{location}$, from the average first-arrival time measured at a given geophone depth from a particular source location, $\bar{t}^{geophone}_{location}$, as

$$\Delta t^{shot,geophone}_{location} = t^{shot,geophone}_{location} - \bar{t}^{geophone}_{location}. \qquad (13)$$

There are 17 curves for each source location corresponding to the 17 effective shotpoints. Shotpoint 1 corresponds to receiver depths of 2550-2500 ft, and shotpoint 17 corresponds to receiver depths of 1580-1540 ft. Each curve is offset from adjacent curves by 5 ms. The vertical dashed lines indicate zero traveltime deviation from the average.

A common shot static is implied for curves that are shifted from their zero lines. Common shot statics are obtained as the intercept of a least-mean-squared-error fit to

each curve, $\Delta t^{shot}_{location}$, and are indicated by the long tic marks at the top of each panel. The common shot statics for all four surface source locations are on the order of

$-3 \text{ ms} < \Delta t^{shot}_{location} < 3 \text{ ms}$.

First-arrival times are required to invert for the interwell velocity model. Seismic data quality is hampered by coherent and random noise, Δt_{noise}, and common shot statics. Timing uncertainties due to Δt^{rec}_{depth} are assumed to be asbsorbed into $\Delta t^{shot}_{location}$. Bulk time-shifts related to $\Delta t^{bulk}_{location}$ are yet to be addressed.

A cross-section view of the acquisition geometry and the first-arrival times, after application of the common shot statics, are shown in Figure 12. Traveltimes to the near receiver well for each source location (the secondary source times) are dashed. Traveltimes to the respective far receiver well are shown as solid curves. The differential traveltimes between the near and far wells varies from roughly 40-80 ms. In the context of the TVSC algorithm, the traveltimes to the far well from each source location are the data to predicted.

The acquisition geometry shows that the raypath coverage is suboptimal. Valid data for the interwell inversion are the first arrivals having raypaths that intersect both receiver wells.

The Initial Velocity Model

A sonic log from the test site covers the depth range from 500-1500 ft. Overall quality of the sonic log is poor. The log does show an overall trend from 6000 ft/s at 500 ft depth to 7000 ft/s at 1500 ft depth. A weathered layer is included at the surface of the initial velocity model. The weathered layer is 200 ft thick and has a velocity of 2000 ft/s. The initial velocity model is taken to be laterally invariant, having a velocity of 6000 ft/s at the base of a weathering layer and increasing with depth to 7500 ft/ sec at 3000-ft depth.

The initial velocity model is shown in Figure 13 along with the data misfit between the observed first-arrival times and the times predicted by surface-source downhole-receiver raytracing through this initial velocity model. Each subpanel contains four curves with each curve showing the data misfit as a function of receiver depth for the respective source location. The curves are color coded to correspond with the source locations indicated above the velocity model. A histogram of the data misfit for each receiver well is also shown.

The weathered-layer model reproduces the general slope of the first-arrival times and predicts the data to within +/- 10 ms. There is a significant DC component to the misfit of the data from source A recorded in well 2. This DC component may be a result of errors in the initial velocity model, or in $\Delta t^{bulk}_{location}$. Parameterization of the weathered layer is completely arbitrary due to the lack of a priori information but partially compensates for the unknown overall $\Delta t^{bulk}_{location}$ associated with the air guns.

Despite applying the shot static corrections, noise is apparent in the first-arrival times. Discontinuities that occur at 50 ft intervals (six depths) are evident. These discontinuities correlate with movement of the hydrophone arrays uphole. These timing variations are noise in the data. The average traveltime difference of the reference and observed times is roughly 50 ms. Noise as large as +/-5 ms is present in the secondary source times and in the observed times, and is a significant portion of this traveltime difference. The fact that noise is present in the secondary-source times means that errors are introduced into the forward modeling. Consequently, the inversion results will be biased by this modelization noise.

Raypath coverage obtained by raytracing from the surface source locations through the initial velocity model to the downhole receivers in the respective observation well is shown in Figure 14. Raypaths that intersect the reference well are valid in the context of the TVSC algorithm. Raypaths that do not intersect the reference well cannot be used in the inversion. No source location has all raypaths to the observation well intersecting the reference well. Source locations B and C are especially lacking.

The TVSC approach as applied to the real data is sensitive to the initial velocity model. Blakeslee et al. (1993) and Blakeslee (1994) state that the ideal TVSC experiment has raypaths from all surface sources intersecting both receiver wells. If this occurs, the TVSC inversion is independent of the velocity field outside of the interwell space since the differential traveltimes between the wells are used.

TVSC Inversion results

Theoretically, the TVSC approach is not dependent on the velocity field that lies outside of the interwell space. These components of the velocity field do, however, influence the raypaths that can be used in the TVSC inversion since the range of recorded depths do not encompass all raypaths. Well 2 is the observation well for sources A and B, while well 1 is the observation well for sources C and D. Useable depth ranges of data

are 1850-2550 ft for source A, 2450-2550 ft for source B, 2090-2550 ft for source C, and 1760-2550 ft for source D.

The earth model is 1100 ft in depth by 700 ft in the horizontal dimension. This model is parameterized with 10 B-spline nodes in the x-dimension, and 50 nodes in the z-dimension. There are 500 model parameters to be estimated in the inversion. The initial model parameters $\mathbf{m}_{\text{prior}}$ are the B-spline coefficients, c_{ij}, that describe the initial velocity model.

Contributions to $\underline{\mathbf{G}}^T\underline{\mathbf{G}}$ and $\underline{\mathbf{G}}^T\Delta\mathbf{d}$ (from equation 11) are calculated concurrently as each ray is traced. Since there are 500 model parameters, $\underline{\mathbf{G}}^T\underline{\mathbf{G}}$ is 500 by 500 in size, as is $\underline{\mathbf{C}}_m^{-1}$. After each iteration, the model parameter updates are added to the prior model parameters (equation 11). The updated model is then used to calculate the updated data misfit $\Delta\mathbf{d}$, $\underline{\mathbf{G}}^T\underline{\mathbf{G}}$, and $\underline{\mathbf{G}}^T\Delta\mathbf{d}$.

Inversion results where low and high noise levels have been assumed for the data are shown in Figures 15 and 16. Velocity estimates after each of three iterations are shown in Figure 15. In Figure 15b, the data are assumed to contain noise so σ_d^2 is four times larger than in Figure 15a. The full form of $\underline{\mathbf{C}}_m^{-1}$ is used.

The basic form of the velocity model is estimated after one iteration. The dipping interface of the high velocity region is apparent. Velocities in the deeper portion of the interwell space are modified in later iterations. Higher spatial frequencies are included in the velocity estimates seen in Figure 15a due to the decreased influence of $\underline{\mathbf{C}}_m^{-1}$. Smoothing is introduced into the velocity estimates by increasing σ_d^2 (Figure 15b). An overall velocity increase from approximately 6800 ft/s at 1540 ft depth to 7600 at 2550 ft depth is apparent. A sharp velocity increase occurs at roughly 2000 ft depth, below which the velocities are relatively constant. Lateral velocity variations seen in Figure 15a are likely produced by the noise in the data, and by noise in the secondary source traveltimes.

The initial and final data misfit (after the third iteration) are shown in Figure 16. Raypaths that arrive at the observation well and intersect the receiver well within the depth range of the receivers are used in the inversion and are shown. Most of the misfit values are within +/- 5 ms, and the misfit is slightly larger in the high-noise case. This is expected since the increased effect $\underline{\mathbf{C}}_m^{-1}$ of produces a smoother velocity estimate. This issue of model smoothness and reasonableness versus degree of data misfit is fundamental in all types of tomographic inversions.

In general, the results should be interpreted in terms of true geology until proven otherwise. However, considering the noise present in the first-arrival time data, the

reasonableness and simplicity of the velocity model, and the final data misfit, the preferred velocity estimate from the real data inversion is Figure 15b.

Inversion results: VSP Traveltime Inversion

TVSC results can be compared with traveltime inversion results obtained assuming a conventional VSP geometry. Source-receiver offsets are now required, whereas they are not needed for TVSC tomography. The earth model parameterization consists of 20 B-splines equally spaced over 6000 ft in the x-dimension, and 25 B-splines equally spaced over 2600 ft in the z-dimension. The spacing between B-splines is greater than in the TVSC inversion, thus, the resulting velocity estimates will be lower spatial frequency. Weighting parameters for the inversion, $\underline{C}_m^{-1}$, λ_1, λ_2, λ_3, λ_4, are identical to those used in Figures 15b and 16b (the high-noise case).

The final velocity model after three iterations is shown in Figure 17 as is the final data misfit. The inversion has modified the initial velocity model so that the data misfit histograms are now centered around zero misfit with the data predicted to within +/- 5 ms.

The final velocity estimates obtained from the TVSC and surface tomography inversions are shown in Figure 18. A histogram summarizes the velocity misfit between the interwell and surface tomography inversions. Effectively fewer B-spline coefficients in the interwell region and less susceptibility to noise both contribute to the lower spatial frequency results obtained from surface-source tomography. The 7200 ft/s contour is slightly shallower in the surface tomography result. Given the different B-spline parameterizations, the noise present in the TVSC data, and the arbitrary specification of the weathered layer, the velocity estimates are reasonably similar.

The data are predicted to within +/- 5 ms (Figure 19) except for the traveltimes from source D in the 2240-2460 ft depth range. Only shown are the data included in the TVSC inversion. Recall that source D has the poorest signal-to-noise ratio and the largest amount of noise in the first-arrival times.

Discussion

The TVSC algorithm actually approximates the true raypaths. The true raypath from the source to the observation well is approximated as a portion from the source to

the near-receiver well, and then as a portion between the wells. This is true even for a velocity model that is known exactly. The error induced by this approximation is not necessarily uniform for all receiver depths and will be influenced by the receiver depth spacing. Slight errors in the predicted traveltimes result.

The most suitable model parameterization is dependent on the prior expectation about the geologic model and the data. Most crosswell tomography applications have used a cell representation for the velocity model. A cell parameterization potentially allows all spatial frequencies into the velocity estimates, but unrealistic velocity models often result. Meyerholtz et al. (1989), Philips and Fehler (1991), Bube and Langan (1994), and Wang and Braile (1995) have recognized the importance of $\underline{\mathbf{C}}_m^{-1}$ in obtaining reasonable velocity models from cell-based tomography.

Lazaratos and Marion (1996) parameterize the interwell space as a stack of thin layers. The layering is inferred from sonic logs at the source and receiver wells. Velocities in each layer are described with a velocity node and a gradient. This parameterization, while more geologically reasonable for their data than cells, would not be appropriate for a situation where the interwell region contains geologic structure that is not seen in the sonic logs.

Seismic waves propagate as waves, not as rays. Wavefronts heal as they propagate, and multipathing also introduces a smoothing effect. Researchers have illustrated the failure of ray-trace first-arrival times to accurately predict the first-arrival traveltimes of real crosswell seismic data (Schuster and Quintus-Bosz, 1993; Baina and Podvin, 1994; Mo and Harris, 1994; Vasco et al., 1995). "Rough" velocity models produce head waves (refractions) that may be the true first-arrival according to ray theory, but are not the first-arrivals that contain significant seismic energy. As a result, some smoothing applied to the velocity model, such as that implicit in the B-spline parameterization, to attenuate these head-wave arrivals is justified.

B-splines are inherently a low spatial-frequency parameterization that is well suited for this noisy data set. The number of B-spline coefficients and the specification of $\underline{\mathbf{C}}_m^{-1}$ control the smoothness of the updated velocity model (as does σ_d^2). An interpretive judgment is required in the selection of σ_d^2 and the weighting parameters, λ, of $\underline{\mathbf{C}}_m^{-1}$. The real data examples illustrate the importance of these parameters in achieving a model estimate that fits the data to an acceptable degree and is geologically reasonable and meaningful. Prior information (reliable sonic logs, zero-offset velocity surveys or VSP's), when available, would help to evaluate the reasonableness of the inversion results.

Theoretically, the TVSC approach is not dependent on the velocity model that lies outside of the interwell space. The field data are dependent on the so-called background

velocity since it is the background velocity that determines which raypaths intersect both receiver wells. As shown, the TVSC inversion can still be employed but using only a subset of the raypaths. The real data should have been acquired with a receiver depth range of 2550-800 ft. In addition, a one receiver overlap as the hydrophones are moved uphole during data acquisition would provide data redundancy to better quantitatively evaluate shot reproducibility and timing consistency.

Static shifts due to timing inconsistencies are present in the real data, as they are in all seismic data, to varying degrees. Shot- and receiver-related timing inconsistencies are an issue in the recording and processing of seismic reflection data. Seismic-reflection data analysis usually recognizes the overall bulk-timing inconsistency, which is generally on the order of 30-120 ms depending on whether the data are marine or land. A variety of static corrections are applied to account for source and receiver timing variations produced by a variable near surface. After processing, a bulk static shift is commonly required to tie a well-based synthetic seismogram, or VSP data, to stacked seismic reflection data. This problem is even more important in tomography applications but usually goes unaddressed.

The twin-VSP data quality is hampered by coherent and random noise, Δt_{noise}, and there are common shot statics, $\Delta t^{shot}_{location}$, on the order of +/- 3 ms. Timing uncertainties due to Δt^{rec}_{depth} are neglected. If the source-related bulk time-shift, $\Delta t^{bulk}_{location}$, is the same for all shots at a given source location, then the TVSC approach is independent of this shift since it uses the differential traveltimes between the wells to update the interwell velocities.

The real data inversion suffers from the lack of prior information for the initial velocity model. Inclusion of the weathered layer in the initial velocity model is justified because it meets the prior expectation of a weathered layer on land and approximately accounts for the bulk static shift associated with each source location. The true thickness and velocity of the weathered layer are unknown. The assumed values do result, however, in predicted traveltimes that match the overall trends of the observed first-arrival times.

Timing variations present in the data support the use of a relatively large σ_d^2, use of a $\underline{C}_m^{-1}$ having off-diagonal terms, and the lower frequency B-spline model parameterization. The data covariance matrix $\underline{C}_d$ could be specified in a more general fashion to consider variations in magnitude, and correlations among, the noise present in the data. Incorporation of the more general $\underline{C}_d$ into the surface-source downhole-receiver tomography is relatively straightforward.

TVSC tomography uses traveltimes measured in the near-receiver well as secondary sources. If these data contain noise, the noise appears as errors in the forward modeling. Use of a more general $\underline{C}_d$ to describe characteristics of the data noise is not as clear cut.

Inversion examples show that the significant velocity updates are obtained with a single iteration. Successive iterations produce minor changes in the updated velocities.

The surface-source downhole-receiver tomography results, that include a weathered layer, resemble those obtained from the TVSC inversion. These results are lower frequency since the same number of B-spline coefficients now describe a much larger earth model. In order to maintain the same B-spline spacing as in the TVSC inversion, a total of roughly 11,000 model parameters would be required since the B-spline formulation assumes equal spacing for the spline nodes.

Further evaluation of the TVSC approach on a variety of increasingly complicated and realistic synthetic examples and comparisons with true synthetic crosswell data would be of interest. One could then quantitatively evaluate the merits of the TVSC approach versus conventional crosswell tomography.

The real data inversion results should be considered as a first-iterate obtained under the assumptions and conditions discussed. This model will be modified by better prior information, additional data, and/or improved data quality. Effects of anisotropy on the traveltimes are undoubtedly present and have not been comprehended.

Conclusions

The TVSC algorithm is a viable approach for simulating a crosswell tomography experiment. Surface sources should be positioned so that a sufficient angular aperture of data is acquired. The receiver depth range should be large enough so that all raypaths recorded in the observation well intersect the reference well. The dominant wavelength of data in the TVSC experiment is greater than in the true crosswell environment (lower frequencies, longer travel distances). Resolution is expected to be somewhat less than that achieved by conventional crosswell tomography. It is not clear, however, that higher resolution results are actually achieved in true crosswell tomography as is advertised by many proponents.

Results show that the TVSC algorithm, and all types of tomography algorithms, are susceptible to noise in the data. However, through a judicious and logical choice of model parameters, data covariance, and model covariance, reasonable inversion results can be obtained in the presence of noise.

Analysis of the real data suffers from the lack of prior information on the velocity model. A TVSC experiment applied at a site where valid sonic logs, true crosswell data, and/or zero-offset VSP's is encouraged.

Acknowledgments

The Basic Energy Sciences division of the Dept. of Energy provided funding for this work under DOE Grant No. DE-F603-95ER14504. Critical reviews by Milo Backus and Jeff Paine improved the quality of the manuscript. Texaco graciously provided access to their Humble Test Site.

References

Backus, G., and Gilbert, F., 1969, Constructing P-velocity models to fit restricted sets of traveltime data: Bulletin of the Seismological Society of America, **59**, 1407-1414.

Baina, R.M., and Podvin, P., 1994, Seeking inconsistencies in crosswell seismic tomography: Technical Program, 64th Annual SEG Meeting, Soc. Expl. Geoph., Expanded Abstracts, 54-57.

Bishop, T.N., Bube, K.P., Cutler, R.T., Langan, R.T., Love, P.L., Resnick, J.R., Shuey, R.T., Spindler, D.A., and Wyld, H.W., 1985, Tomographic determination of velocity and depth in laterally varying media: Geophysics, **50**, 903-923.

Blakeslee, S., 1994, Twin-VSP simulation of crosswell data: The Leading Edge, **13**, 252-254.

Blakeslee, Sam, Chen, Sen., Krebs, Jerry and Srnka, Len, 1993, TVSC: Twin VSP simulation of crosswell data, A strategy for low-cost monitoring of EOR processes: 63rd Annual Internat. Mtg., Soc. Expl. Geophys., Expanded Abstracts, **93**, 9-12.

Bois, M., LaPorte, M., Lavergne, M., and Thomas, G., 1972, Well-to-well seismic measurements: Geophysics, **37**, 471-480.

Bregman, N. D., Bailey, R. C. and Chapman, C. H., 1989a, Crosshole seismic tomography: Geophysics, **54**, 200-215.

Bregman, N.D., Hurley, P.A., and West, G.F., 1989b, Seismic tomography at a fire-flood site: Geophysics, **54**, 1082-1090.

Bube, K.P., and Langan, R.T., 1994, A continuation approach to regularization for traveltime tomography: Technical Program, 64th Annual SEG Meeting, Soc. Expl. Geoph., Expanded Abstracts, 980-983.

Cerveny, V., and Hron, F., 1980, The ray-series method and dynamic raytracing for three-dimensional inhomogeneous media: Bulletin of the Seismological Society of America, **70**, 47-77.

Coulam, C.M., Erickson, J.J., Rollo, F.D., and James, A.E., 1981, The physical basis of medical imaging: Appleton-Century-Crofts.

Daily, W.D., 1984, Underground oil-shale retort monitoring using geotomography: Geophysics, **49**, 1701-1707.

Dines, K.A., and Lytle, R.J., 1979, Computerized geophysical tomography: Proc. IEEE, **67**, 1065-1073.

Fehler, M., and Pearson, C., 1984, Cross-hole seismic surveys: Application for studying subsurface fracture systems at a hot dry rock geothermal site: Geophysics, **49**, 37-45.

Gustavsson, M., Ivansson, S., Moren, P., and Pihl, J., 1986, Seismic borehole tomography - measurement system and field studies: Proc. IEEE, **74**, 339-346.

Harris, J.M., Nolen-Hoeksema, R.C., Langan, R.T., Van Schaack, M., Lazaratos, S.K., and Rector, J.W., 1995, High-resolutioin crosswell imaging of a west Texas carbonate reservoir: Part 1-Project summary and interpretation: Geophysics, **60**, 667-681.

Herman, G.T., 1980, *Image Reconstruction from Projections: The Fundamentals of Computed Tomography*: Academic Press.

Inoue, H., 1986, A least-squares smooth fitting for irregularly spaced data: finite-element approach using the cubic B-spline basis: Geophysics, **51**, 2051-2066.

Ivansson, S., 1986, Seismic borehole tomography - theory and computational methods: Proc. IEEE, **74**, 328-338.

Justice, J.H., Vassilou, A.A., Singh, S., Logel, J.D., Hansen, P.A., Hall, B.R., Hutt, P.R., and Solanki, J.J., 1989, Acoustic tomography for monitoring enhanced oil recovery: The Leading Edge, **8**, 12-24.

Lazaratos, S.K., Harris, J.M., Rector, J.W., and Van Schaack, M., 1995, High-resolution crosswell imaging of a west Texas carbonate reservoir: Part 4-Reflection imaging: Geophysics, **60**, 702-711.

Lazaratos, S.K., and Marion, B.P., 1996, Crosswell seismic imaging of reservoir changes caused by CO injection: Technical Program, 66th Annual SEG Meeting, Soc. Expl. Geoph., Expanded Abstracts, **96**, 1877-1879.

Lee, D.S., Stevenson, V.M., Johnston, P.F., and Mullen, C.E., 1995, Time-lapse crosswell seismic tomography to characterize flow structure in the reservoir during the thermal stimulation: Geophysics, **60**, 660-666.

Lines, L.R., and LaFehr, E.D., 1989, Tomographic modeling of a cross-borehole data set: Geophysics, **54**, 1249-1257.

Macrides, C.G., Kanasewich, E.R., and Bharatha, S., 1988, Multiborehole seismic imaging in steam injection heavy oil recovery projects: Geophysics, **53**, 65-75.

Mathisen, M.E., Cunningham, P.S., Shaw, J., Vassiliou, A.A., Justice, J.H., and Guinzy, N.J., 1995a, Crosswell seismic radial survey tomograms and the 3-D interpretation of a heavy oil steamflood: Geophysics, **60**, 651-659.

Mathisen, M.E., Vassiliou, A.A., Cunningham, P.S., Shaw, J., Justice, J.H., and Guinzy, N.J., 1995b, Time-lapse crosswell seismic tomogram interpretation: Implications for heavy oil reservoir characterization, thermal recovery process monitoring, and tomographic imaging technology: Geophysics, **60**, 631-650.

McMechan, G., 1988, Seismic tomography in boreholes: Geophysical J. R. Astr. Soc., **74**, 601-612.

Meyerholtz, K.A., Pavlis, G.L., and Szpakowski, S.A., 1989, Convolutional quelling in seismic tomography: Geophysics, **54**, 570-580.

Mo, L., and Harris, J.M., 1994, Calculation of direct arrival traveltimes by the eikonal equation: Technical Program, 64th Annual SEG Meeting, Soc. Expl. Geoph., Expanded Abstracts, **94**, 779-782.

Peterson, J.E., Paulsson, B.N.P., and McEvilly, T.V., 1985, Applications of algebraic reconstruction techniques to crosshole seismic data: Geophysics, **50**, 1566-1580.

Phillips, W.S., and Fehler, M.C., 1991, Traveltime tomography: A comparison of popular methods: Geophysics, **56**, 1639-1649.

Schuster, G. T. and Quintus-Bosz, A., 1993, Wavepath eikonal traveltime inversion: Theory: Geophysics, **58**, 1314-1323.

Squires, L.J., and Cambois, G., 1982, A linear filter approach to designing off-diagonal damping matrices for least-squares inverse problems: Geophysics, **57**, 948-951.

Tarantola, A., 1987, *Inverse Problem Theory*: Elsevier Science Publishing, Inc.

Vasco, D.W., Peterson, J.E., Jr., and Majer, E.L., 1995, Beyond ray tomography: Wavepaths and Fresnel volumes: Geophysics, **60**, 1790-1804.

Wang, B., and Braile, L.W., 1995, Effective approaches to handling non-uniform data coverage problem for wide-aperture refraction/reflection profiling: 65th Annual Internat. Mtg., Soc. Expl. Geophys., Expanded Abstracts, **95**, 659-662.

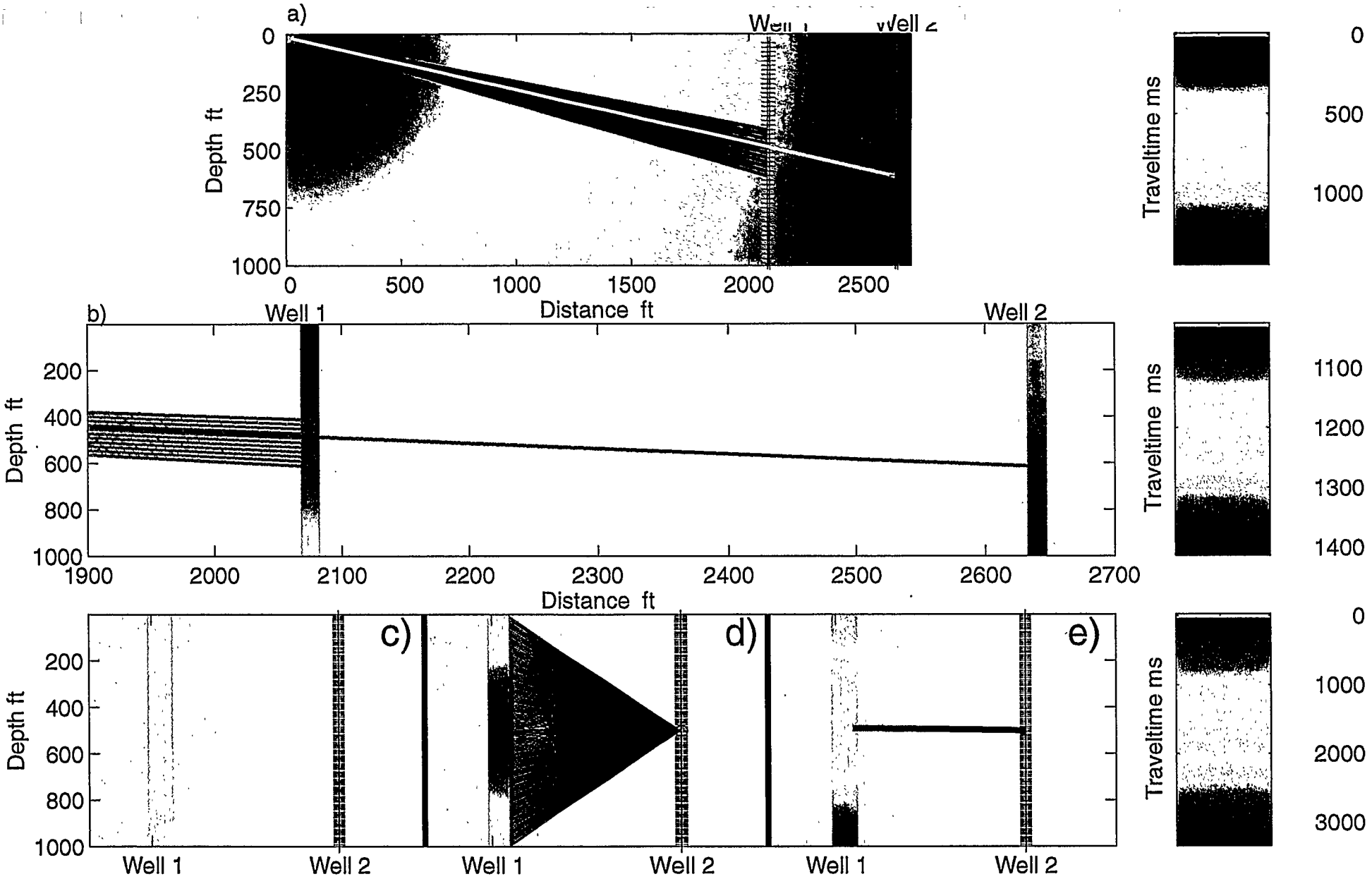

Figure 1: a) Cross section of an earth model showing the traveltime grid (in color) with a single surface source and two receiver wells. Several raypaths from the source to the near receiver well are shown in black along with a single raypath from the source to the far receiver well. b) Expanded view of the interwell region. The actual raypath to the far receiver well is shown in blue. In the context of the TVSC algorithm, the traveltimes measured in well 1 are taken as the reference traveltimes and the objective is to estimate the interwell traveltime such that the reference times added to the interwell times equal the traveltimes measured in the far receiver well (Well 2). c) The reference times in Well 1 are treated as secondary sources and held fixed. d) For each receiver in Well 2, the interwell traveltime to all receivers in Well 1 is estimated and is shown in color. The associated raypaths are also shown. e) The interwell traveltimes estimated in d) are added to the reference times in c) as shown in color in Well 1. The minimum traveltime of the sum is selected as the predicted traveltime for the source to the specified receiver in Well 2.

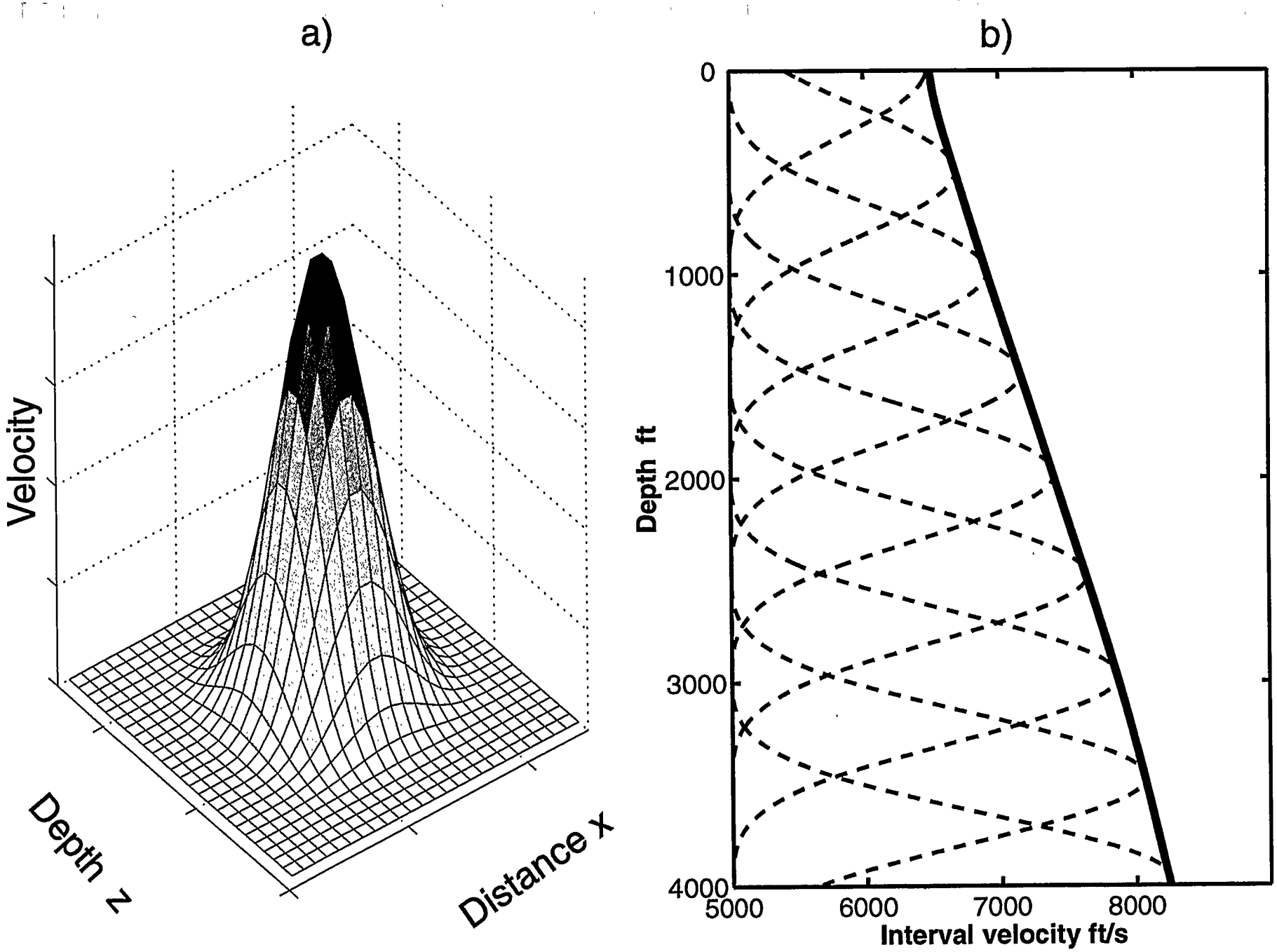

Figure 2: a) Two dimensional B spline basis function. b) A one dimensional profile V(z) at fixed x showing the overlap of the basis functions which superpose to produce a smooth V(z).

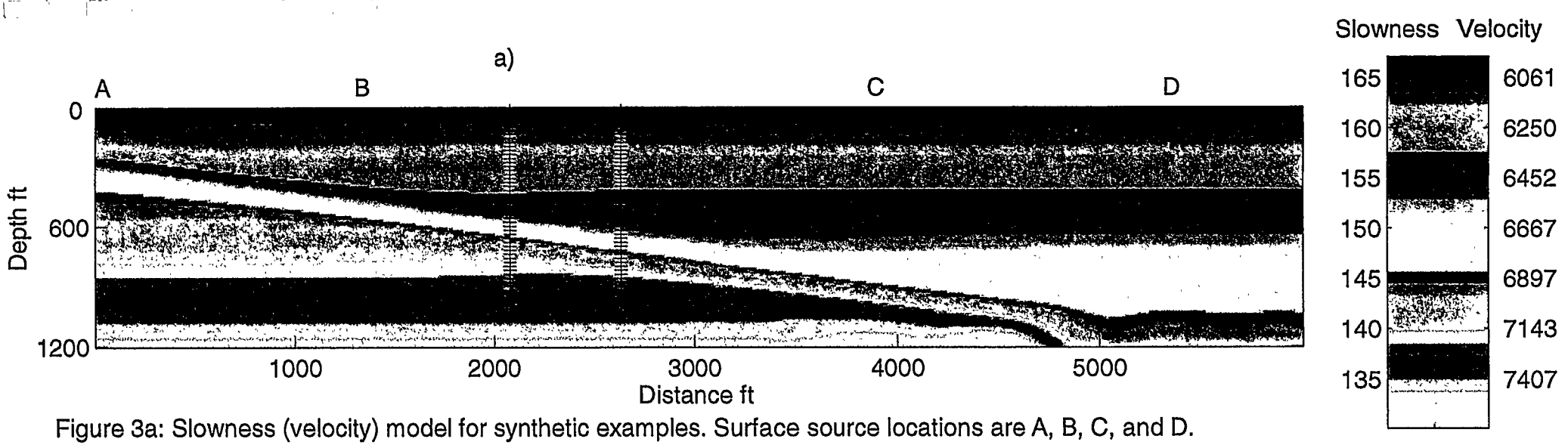

Figure 3a: Slowness (velocity) model for synthetic examples. Surface source locations are A, B, C, and D. The two wells contain receivers from 0 1000 ft depth at a 50 ft spacing. Slowness units are us/ft, velocity units are ft/s.

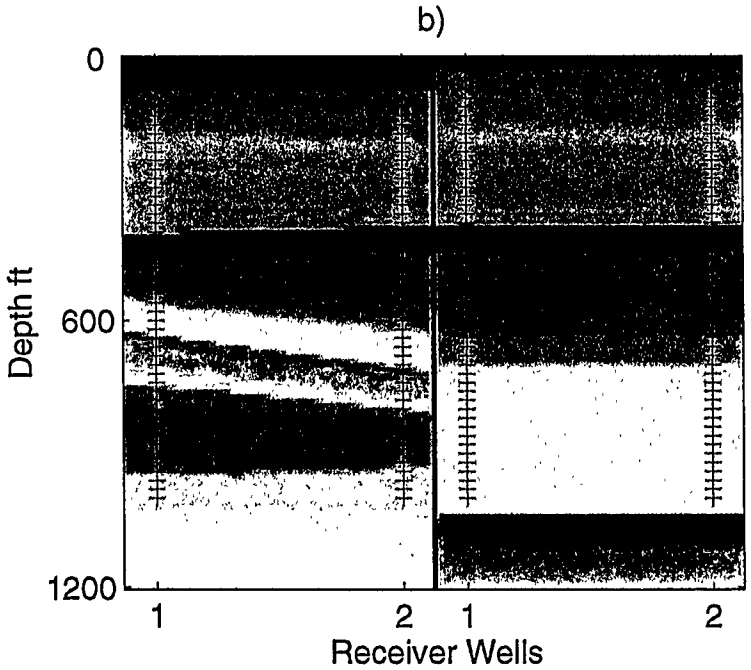

Figure 3b: Closeup view of true and initial slowness (velocity) models.

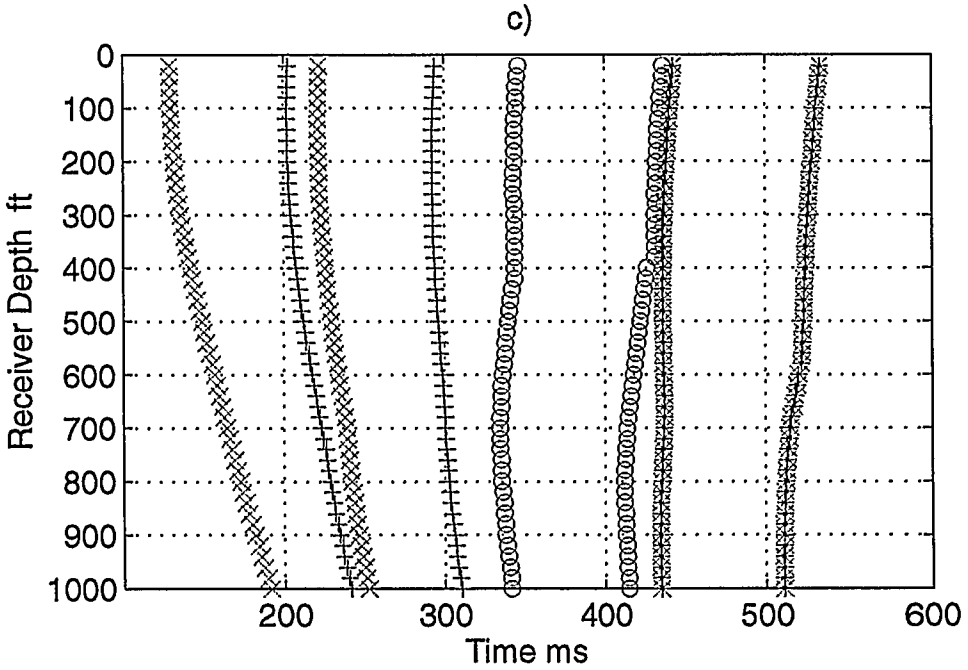

Figure 3c: First arrival times from source locations (A o, B x, C +, D *) to well 1 (red) and well 2 (blue).

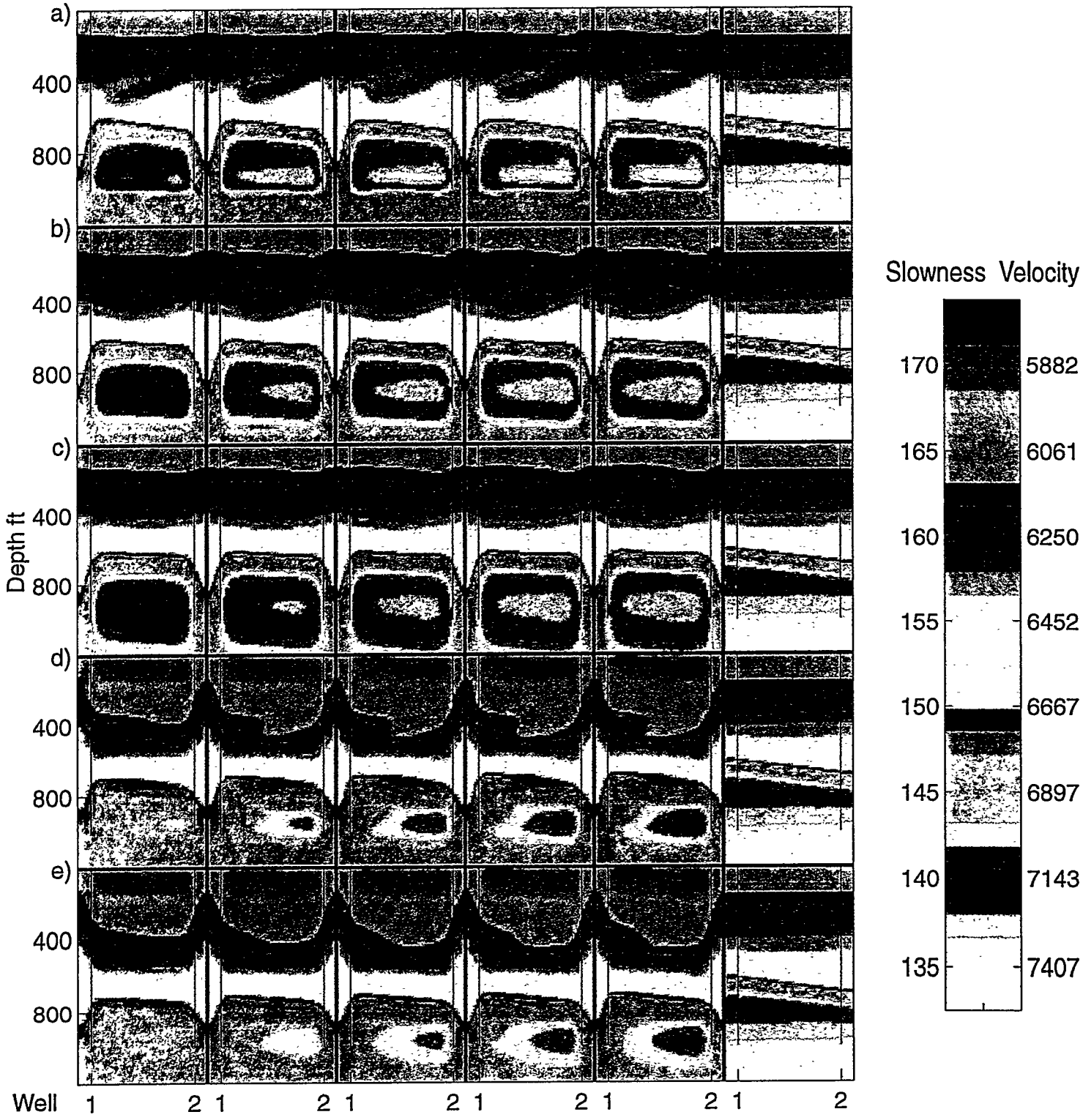

Figure 4: Slowness (velocity) estimates for synthetic examples. Examples a, b, c are the results obtained from the noise free synthetic data. Examples d, and e are obtained from the synthetic data containing noise as shown in Figure 6. In each panel, the result after each consecutive iteration is shown from left to right. The initial model is at the right.

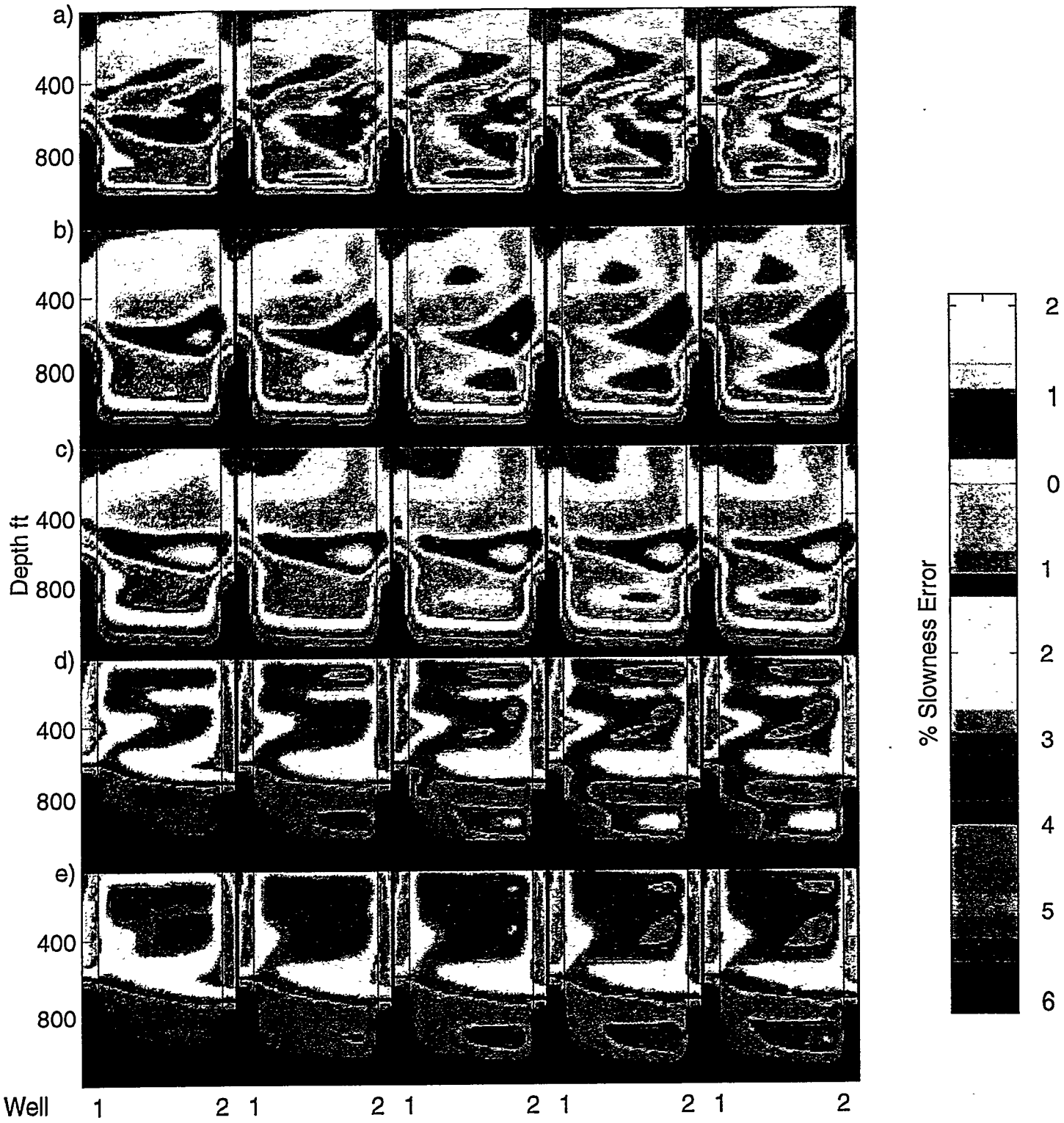

Figure 5: Slowness (velocity) error relative to the true model for the synthetic examples.

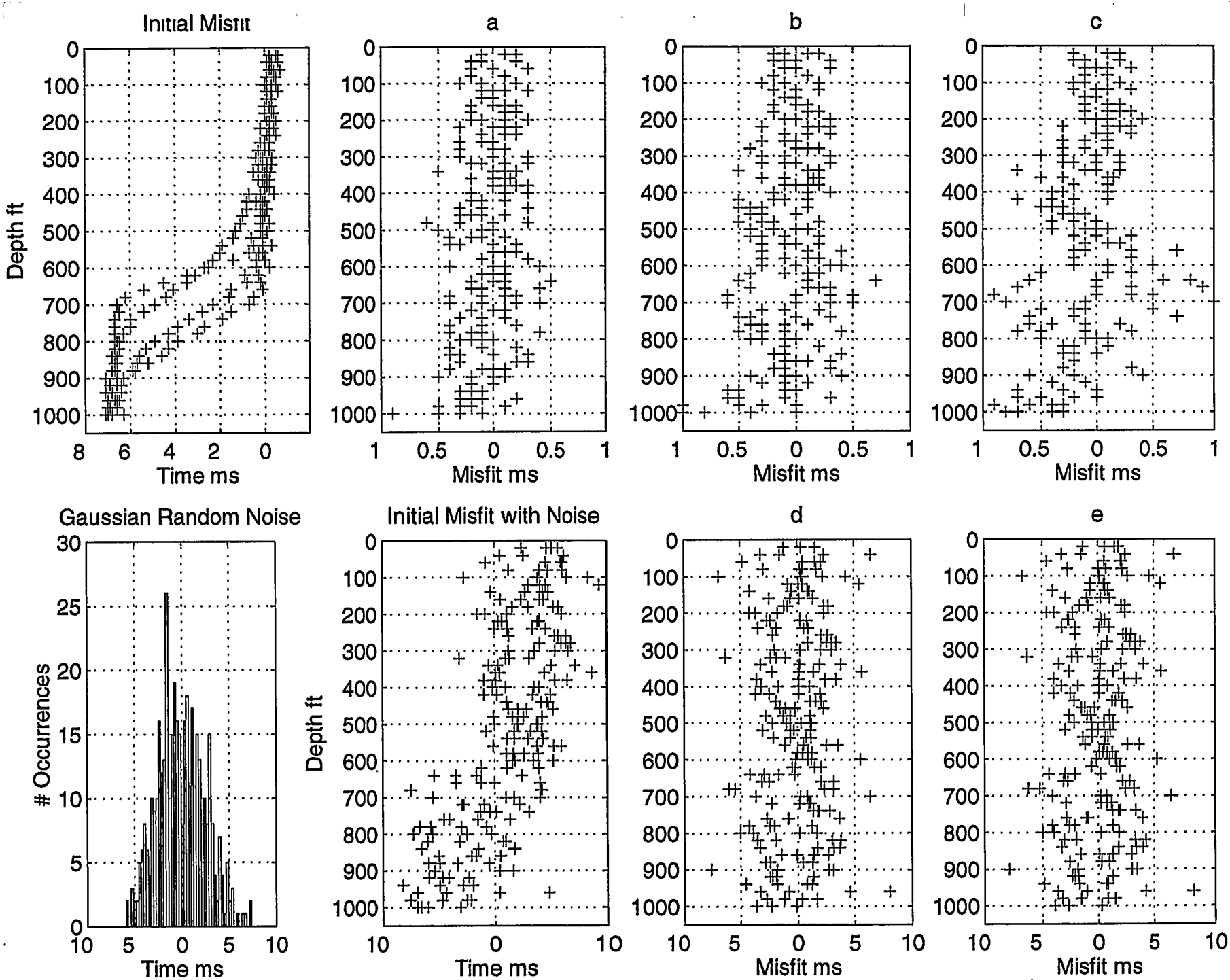

Figure 6: Initial and final data misfit for the noise free examples are shown in the top row. The bottom row shows a histogram of the Gaussian random noise, the initial misfit, and the final misfit for examples d and e.

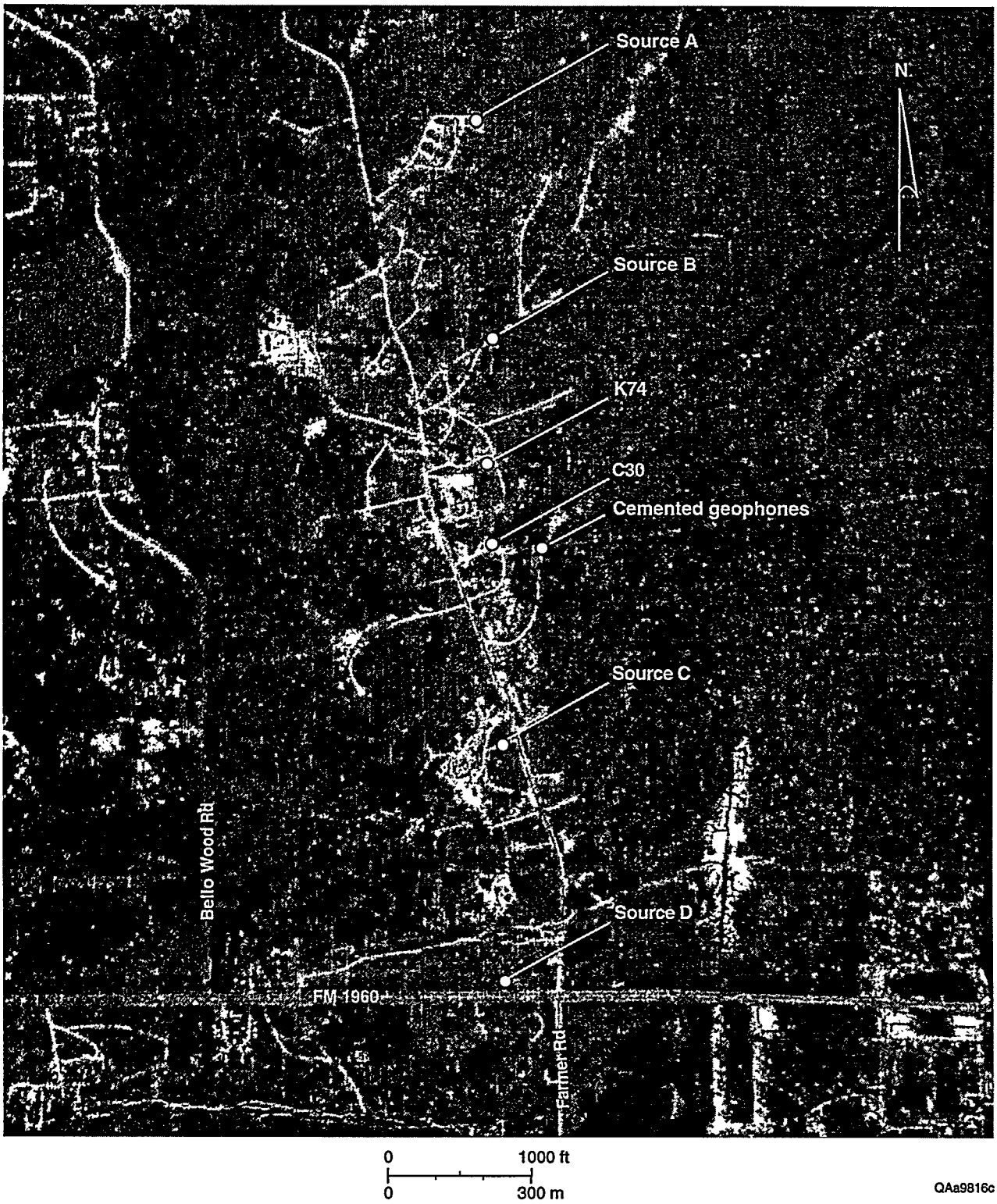

Figure 7: Aerial photograph of Texaco Borehole Test Site in Humble, Texas.

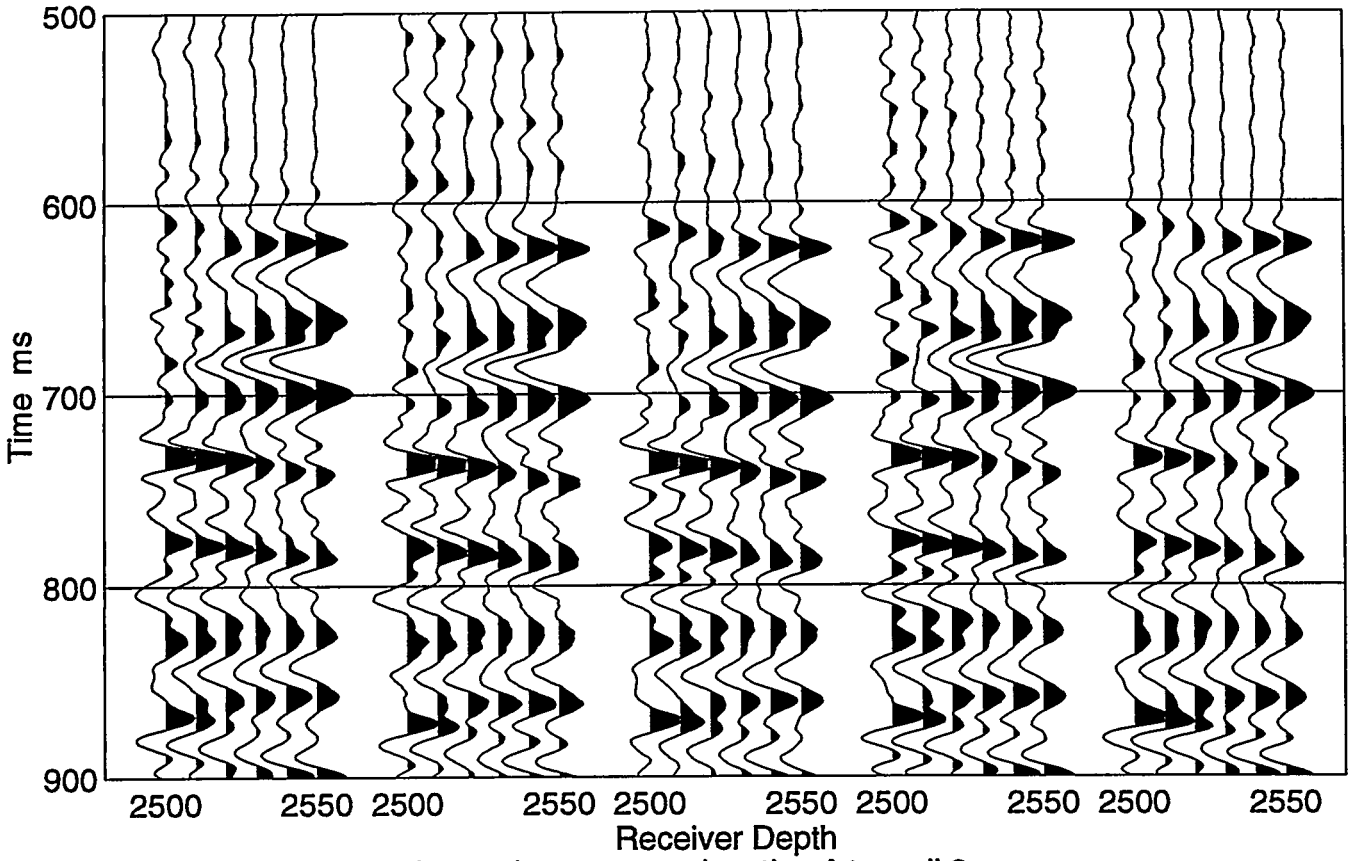

Figure 8a: Common shot gathers, source location A to well 2.

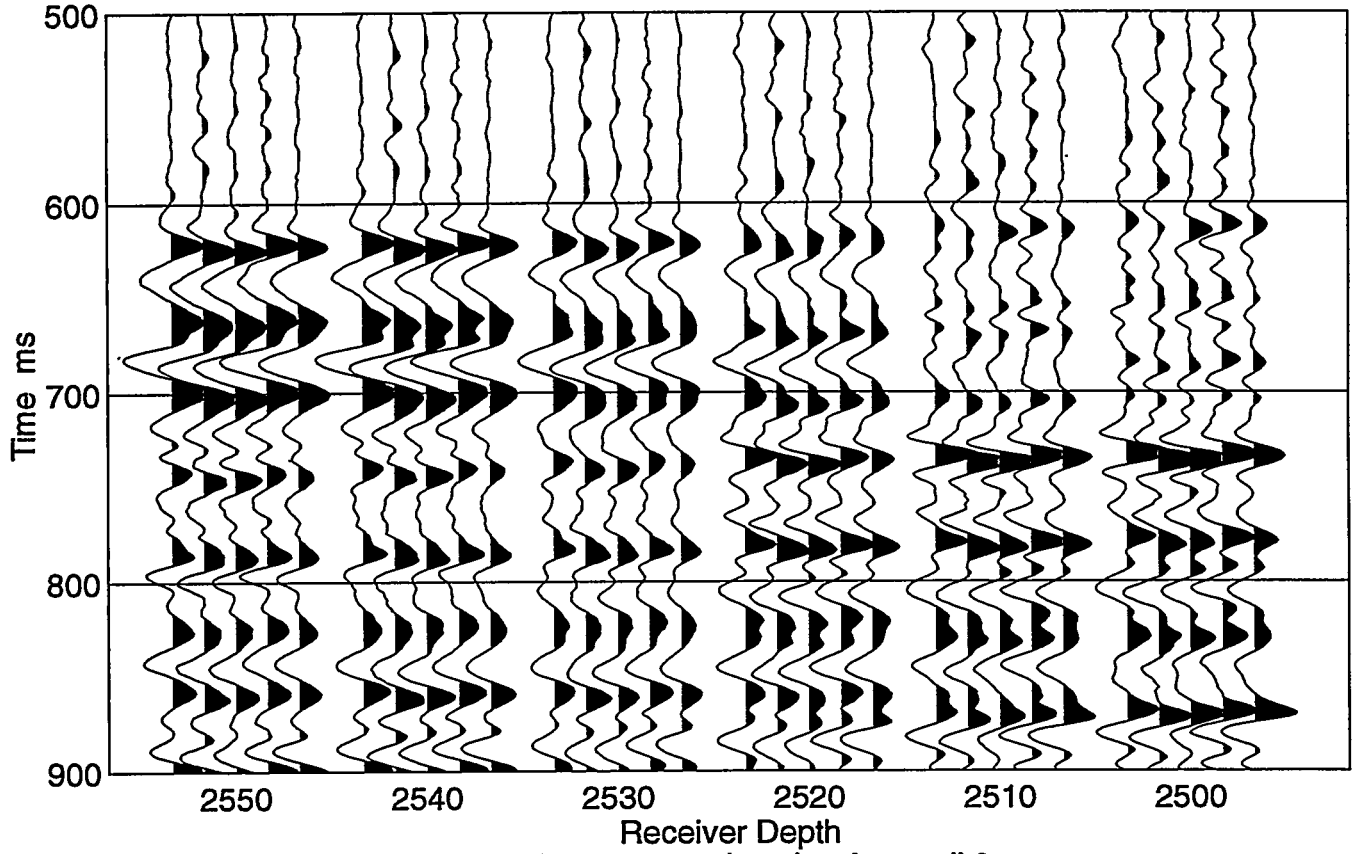

Figure 8b: Common depth gathers, source location A to well 2.

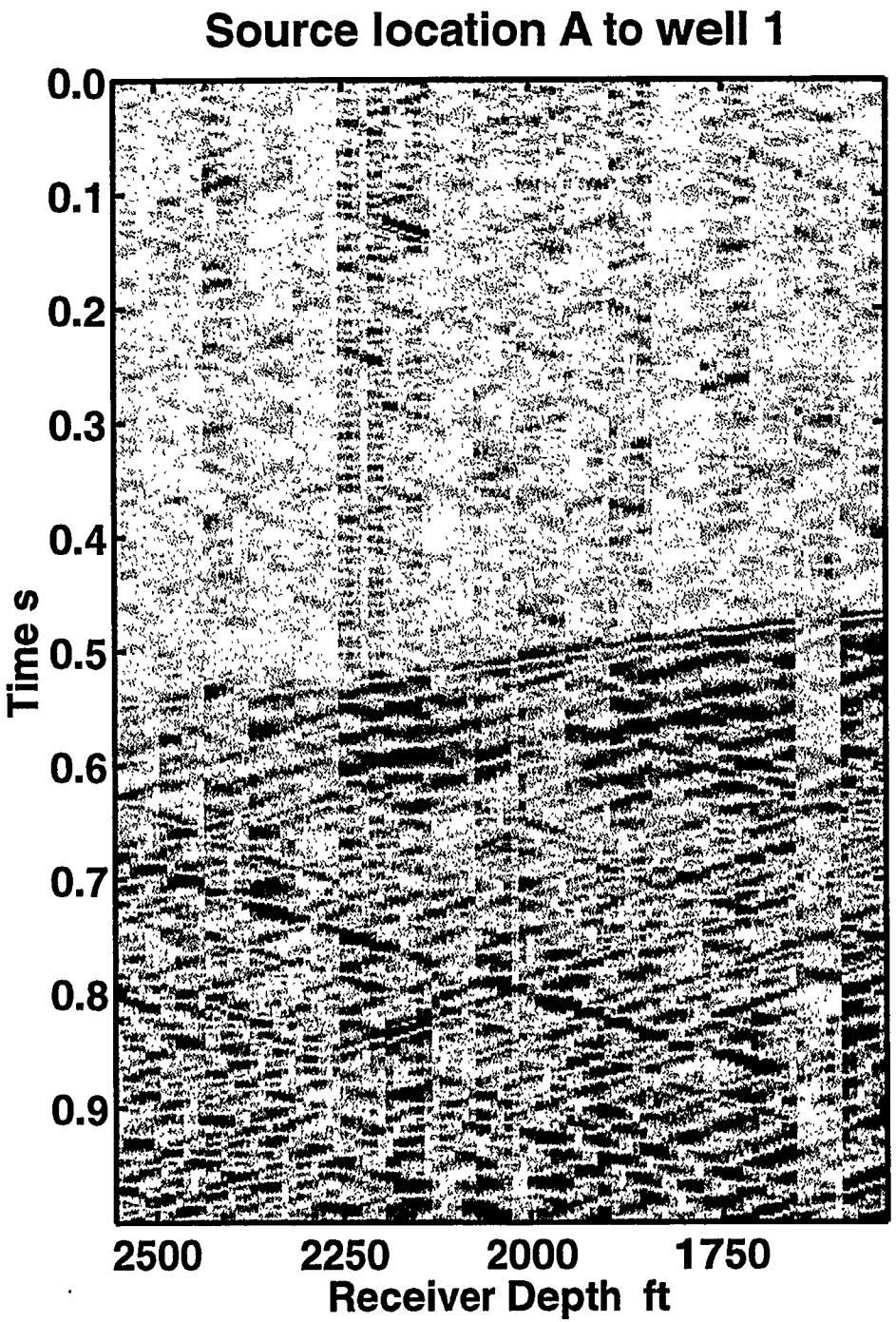

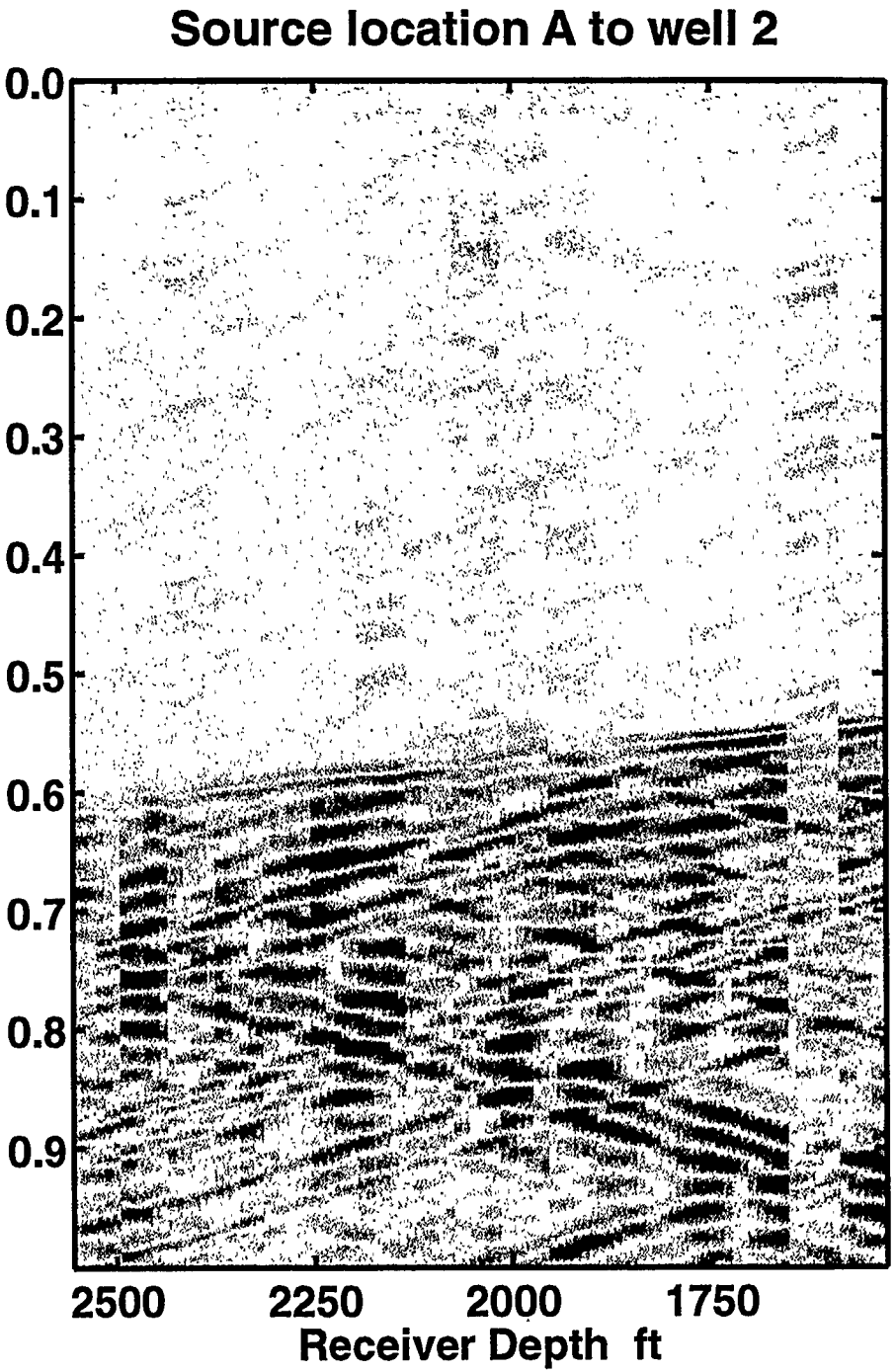

Figure 9a: VSPs, source location A to wells 1 and 2.

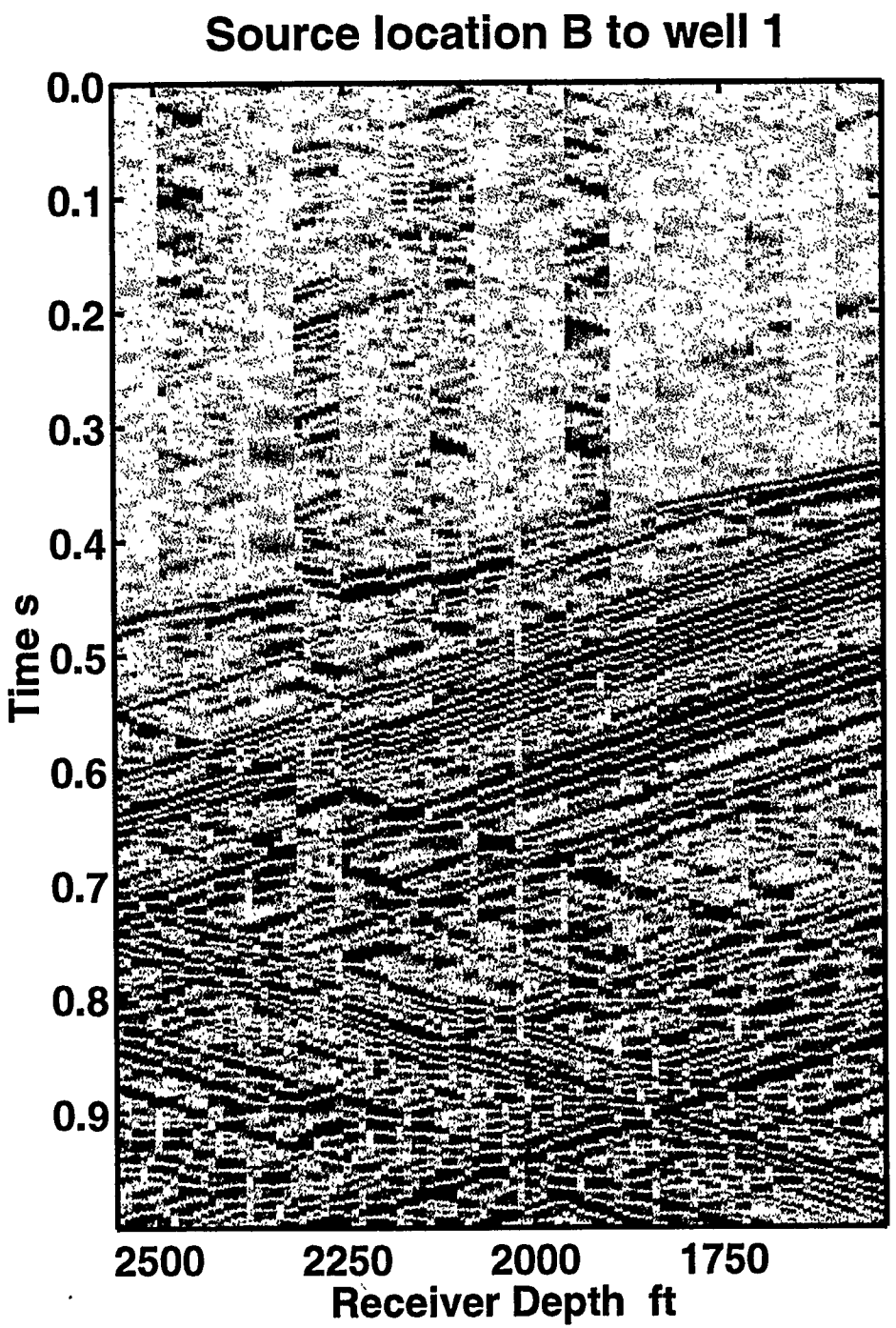

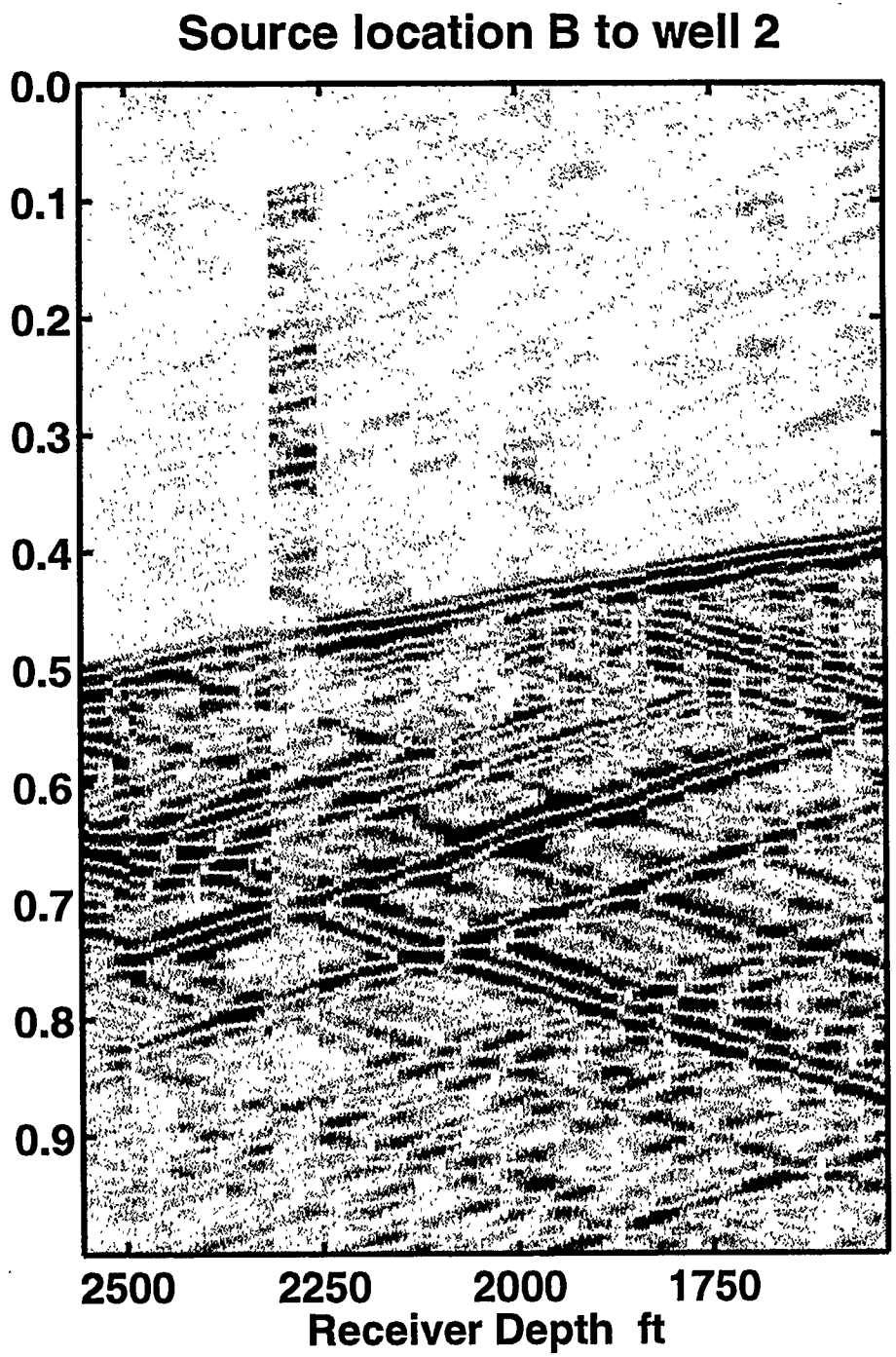

Figure 9b: VSPs, source location B to wells 1 and 2.

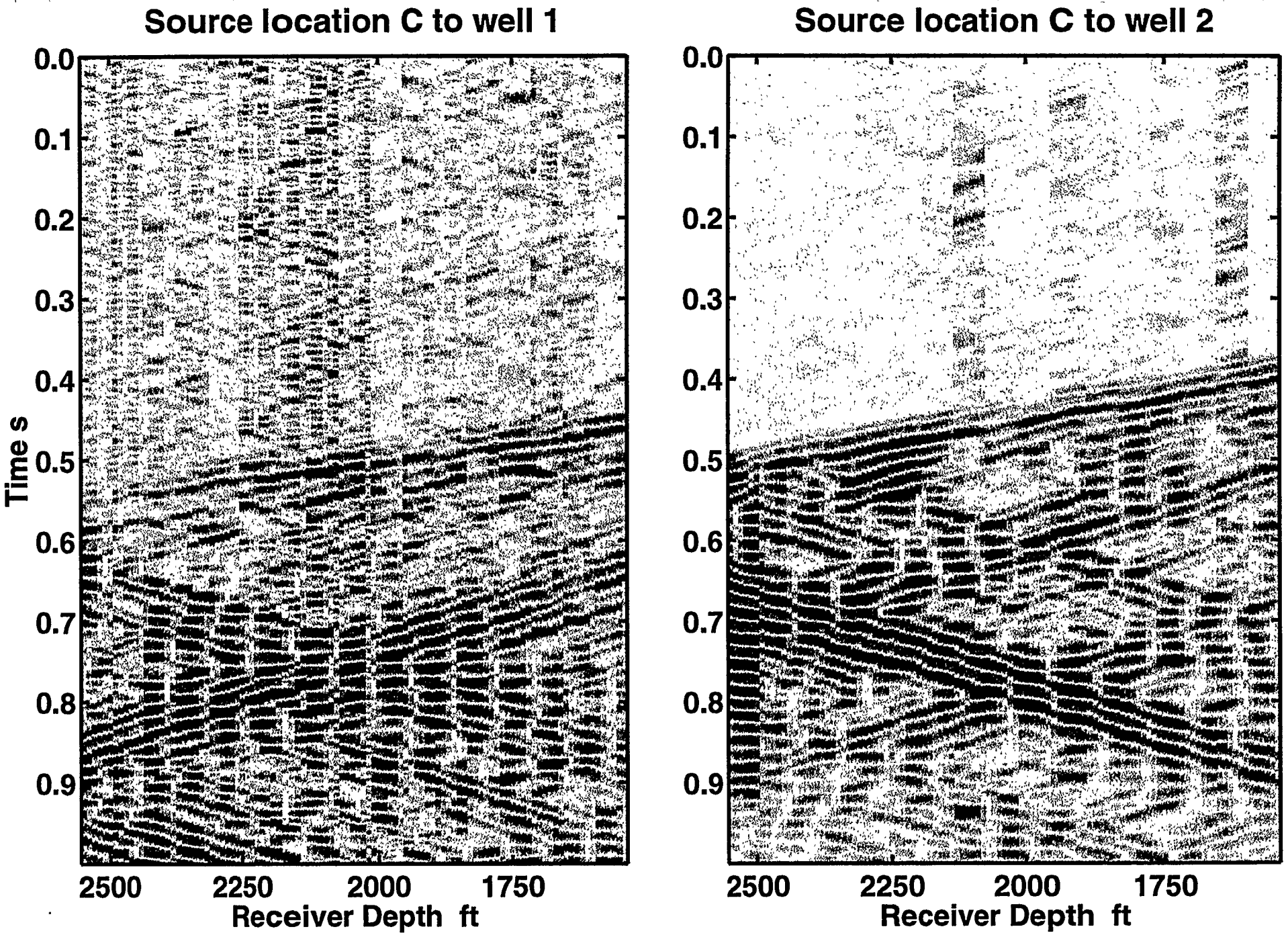

Figure 9c: VSPs, source location C to wells 1 and 2.

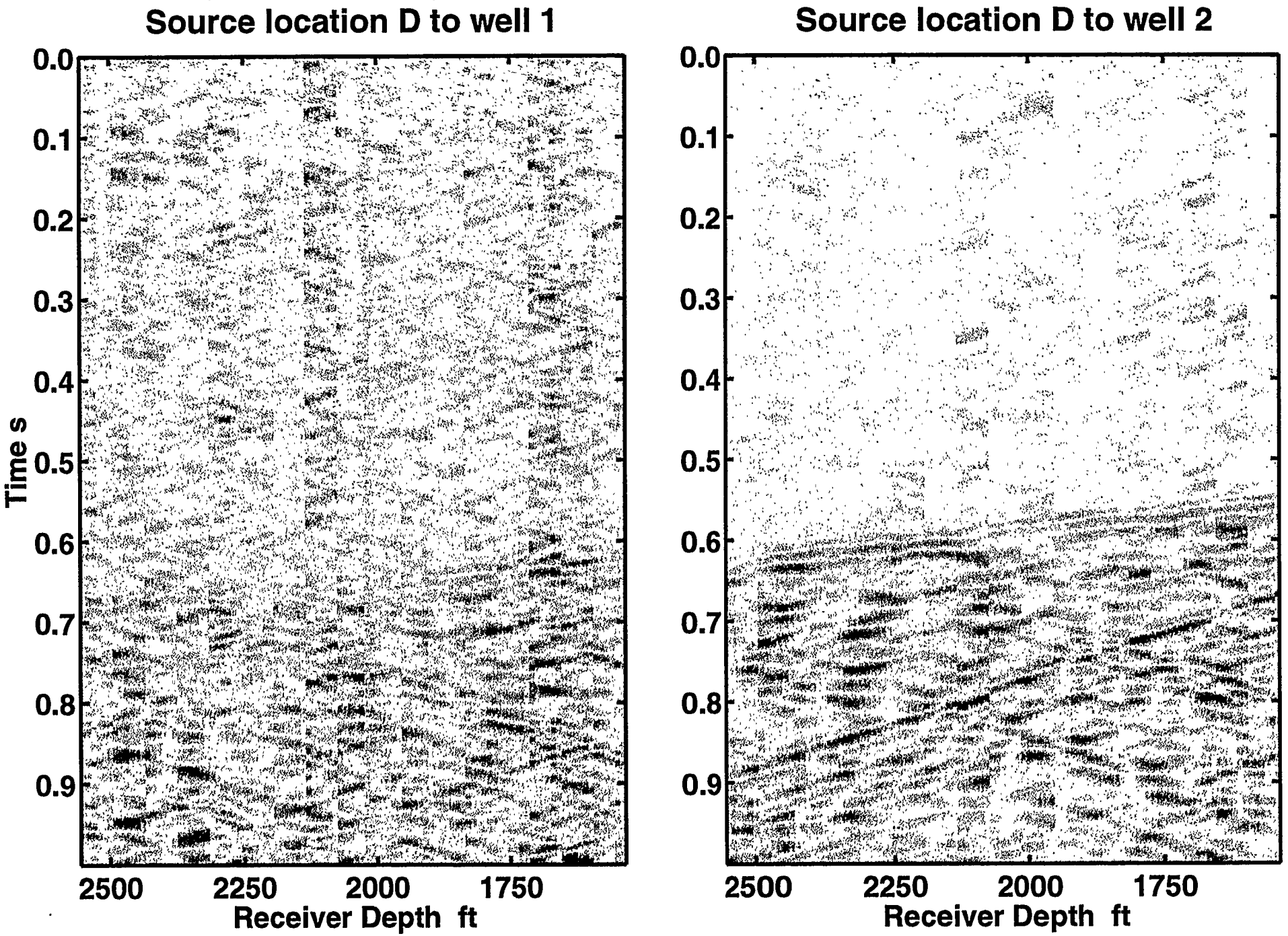

Figure 9d: VSPs, source location D to wells 1 and 2.

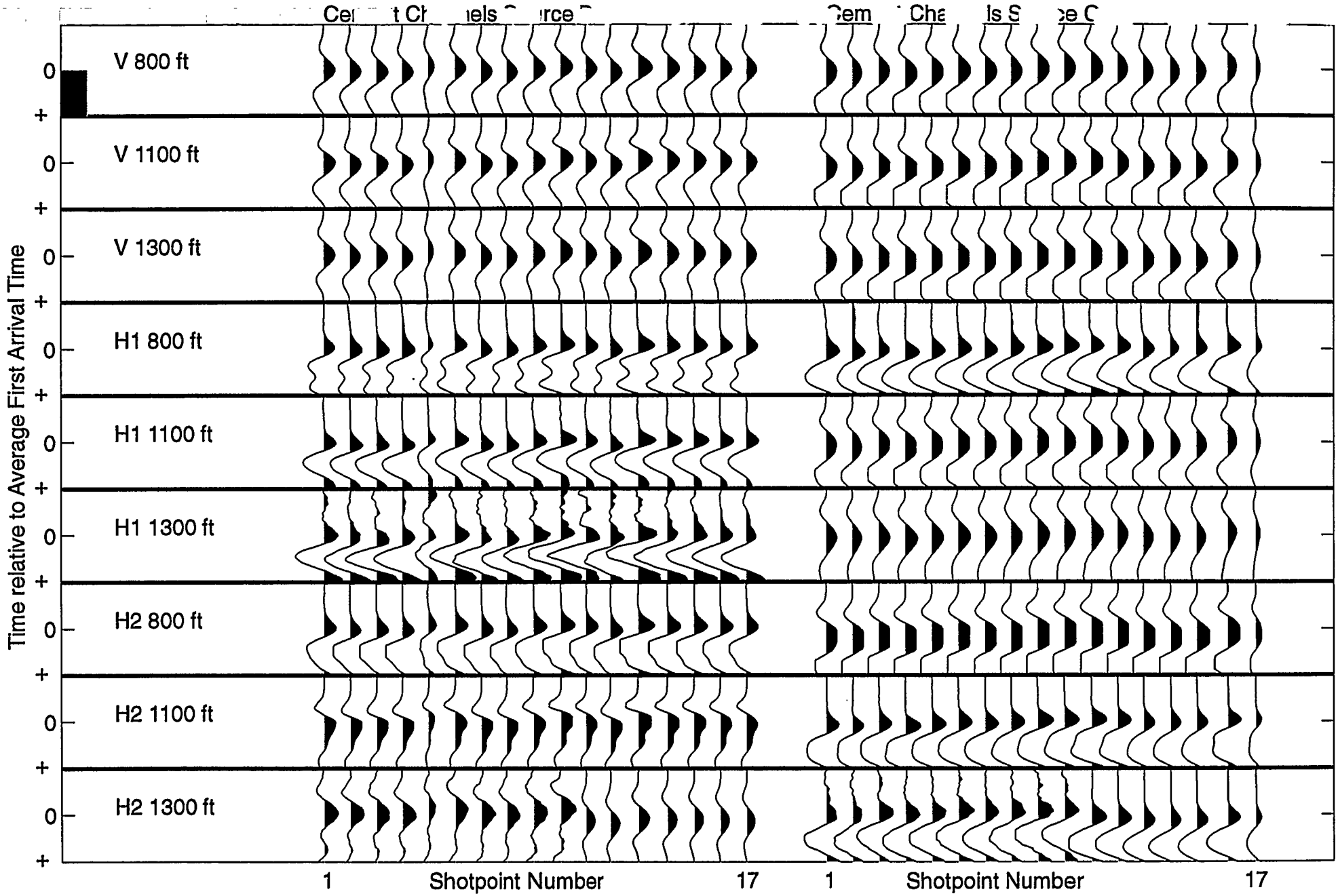

Figure 10: Data from geophones in the cemented receiver well at selected depths. These data have been aligned at their respective average first arrival time. The vertical bar in the upper left denotes 25 ms.

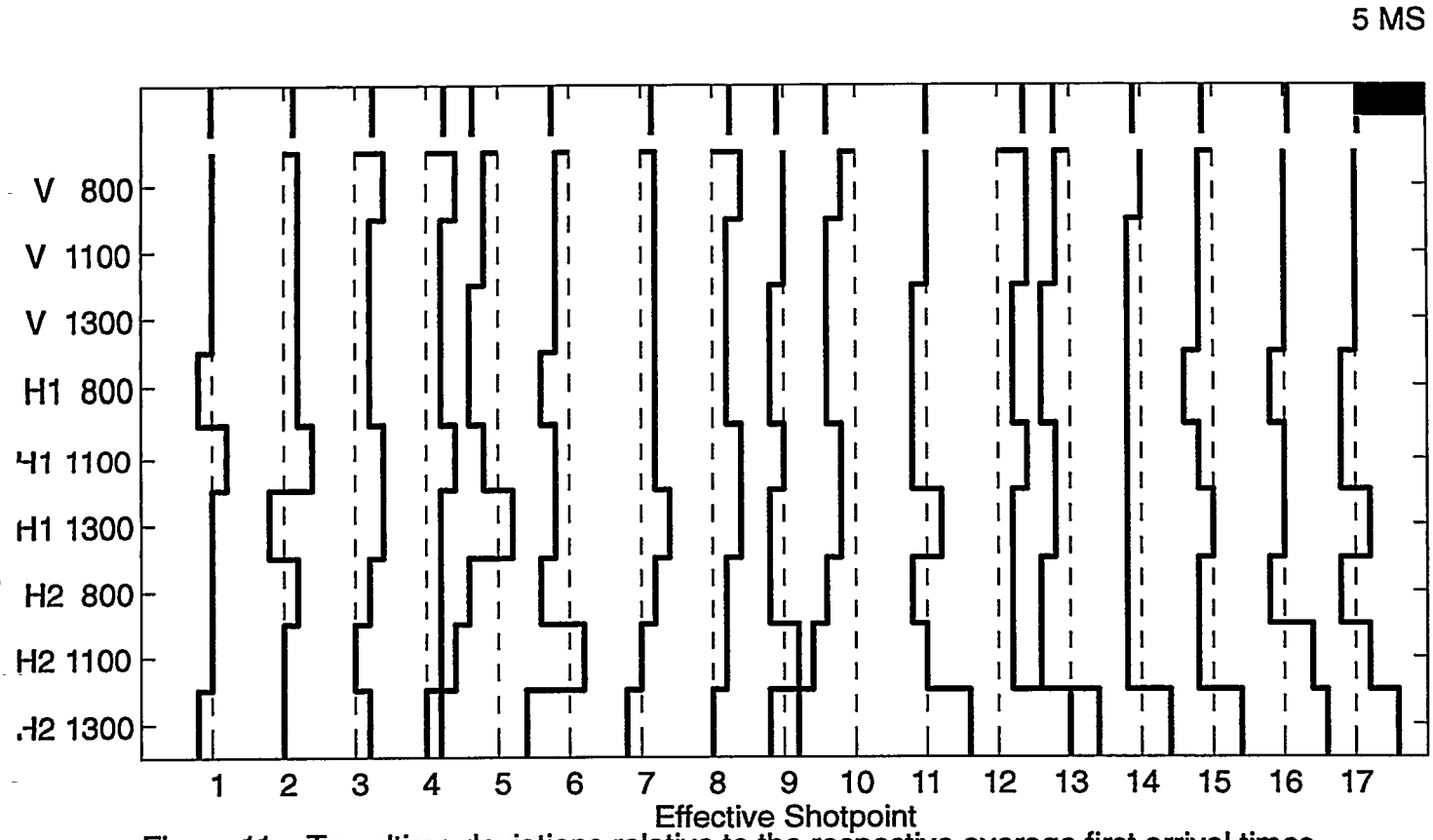

Figure 11a: Traveltime deviations relative to the respective average first arrival times for source B. The vertical bars at the top show the estimated shot static.

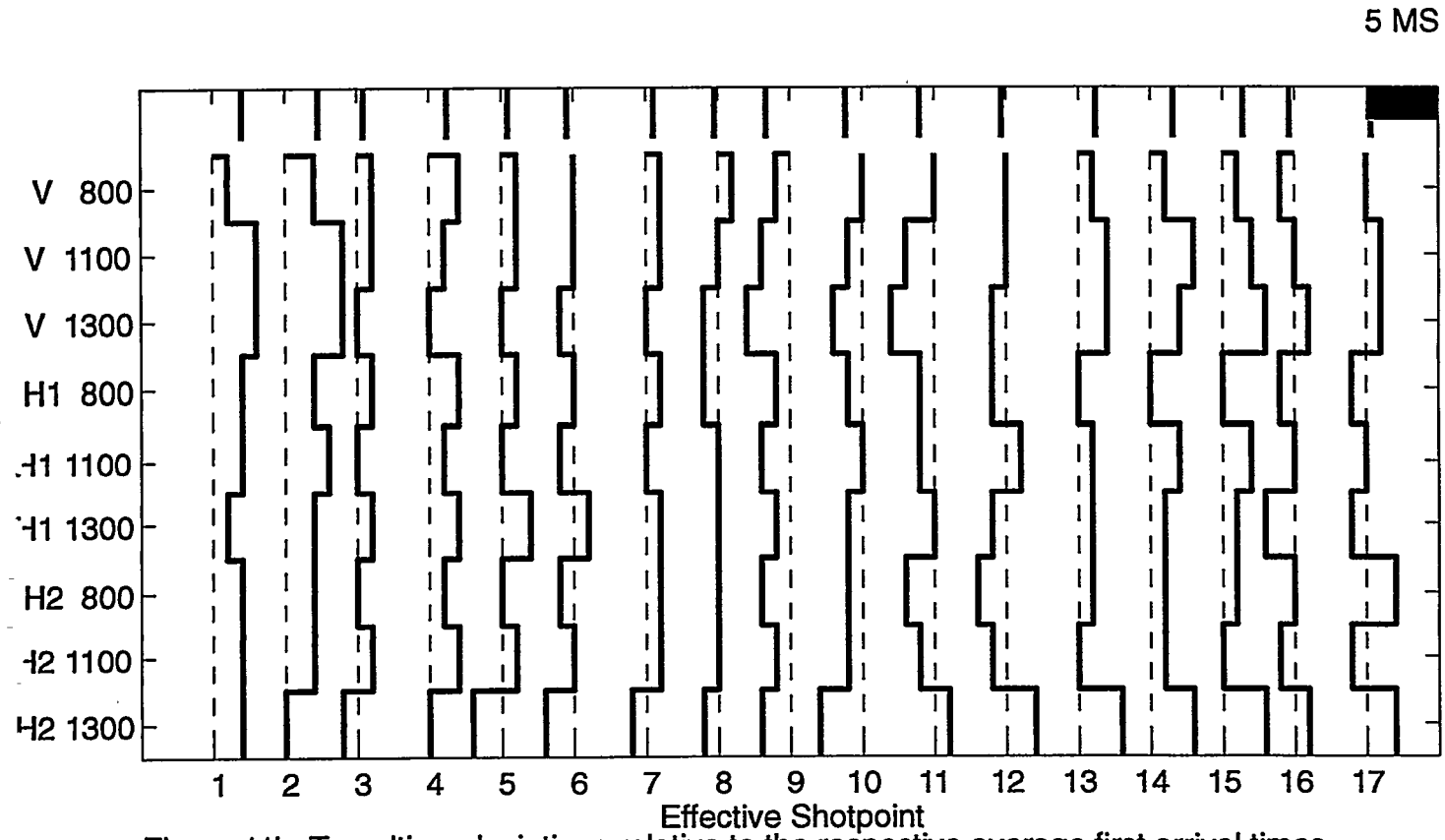

Figure 11b: Traveltime deviations relative to the respective average first arrival times for source C. The vertical bars at the top show the estimated shot static.

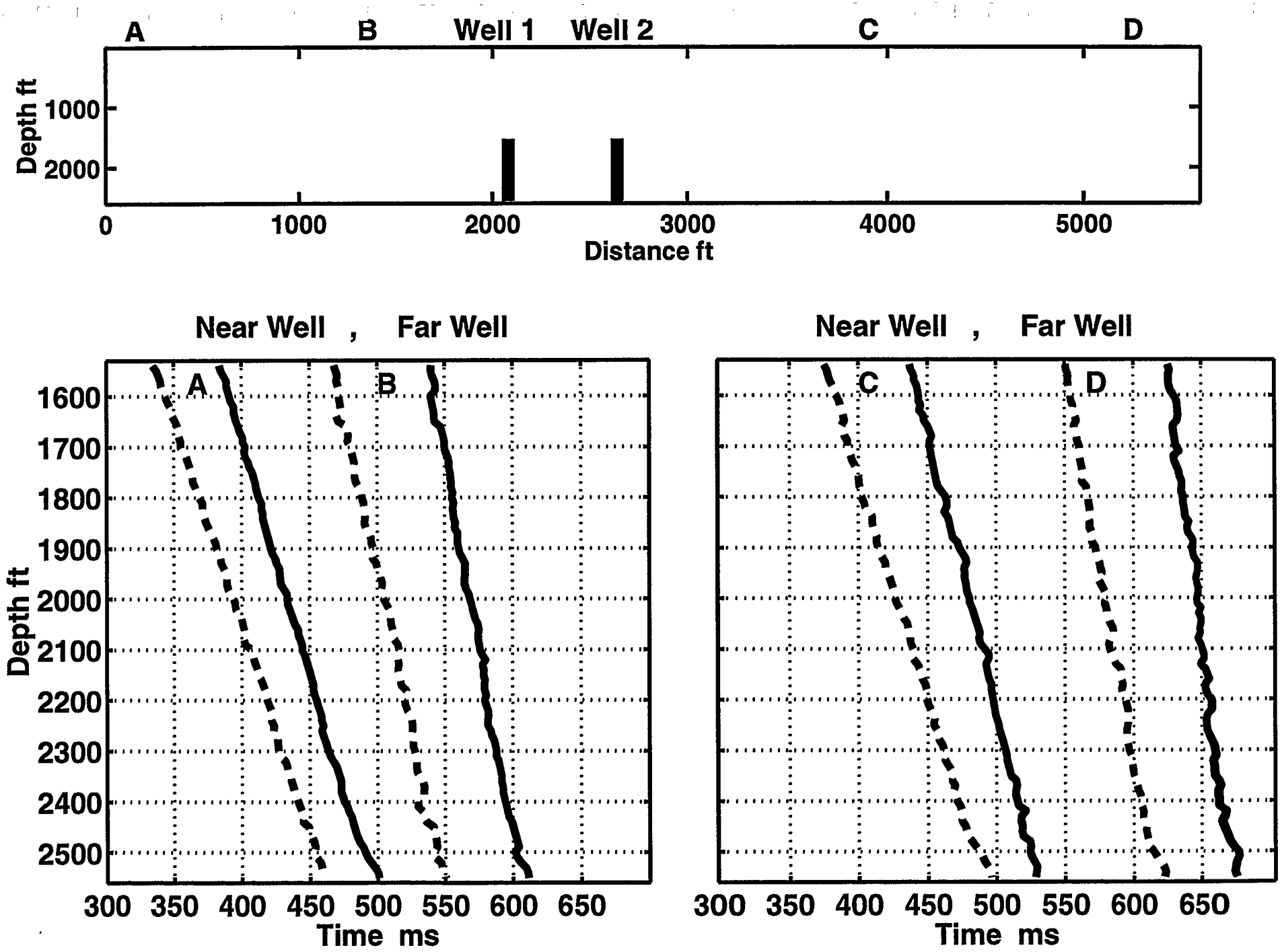

Figure 12: Diagrammatic cross section of the real data acquisition geometry (top). The lower panels show the first arrival times for the indicated source receiver well combinations.

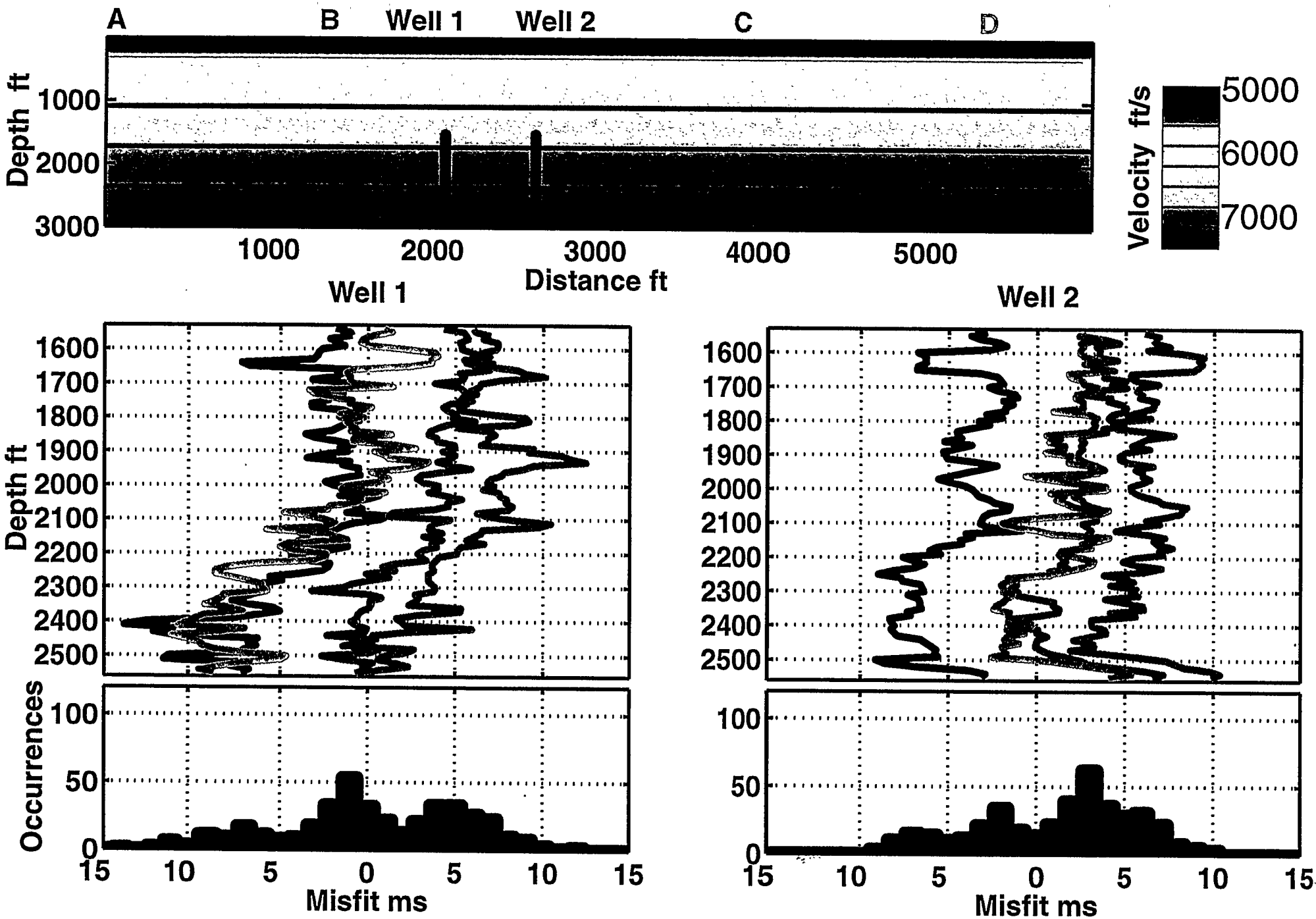

Figure 13: Initial velocity model (top) and initial data misfit for the surface source receiver well tomography. The data misfit as a function of receiver depth is color coded to correspond with surface location.

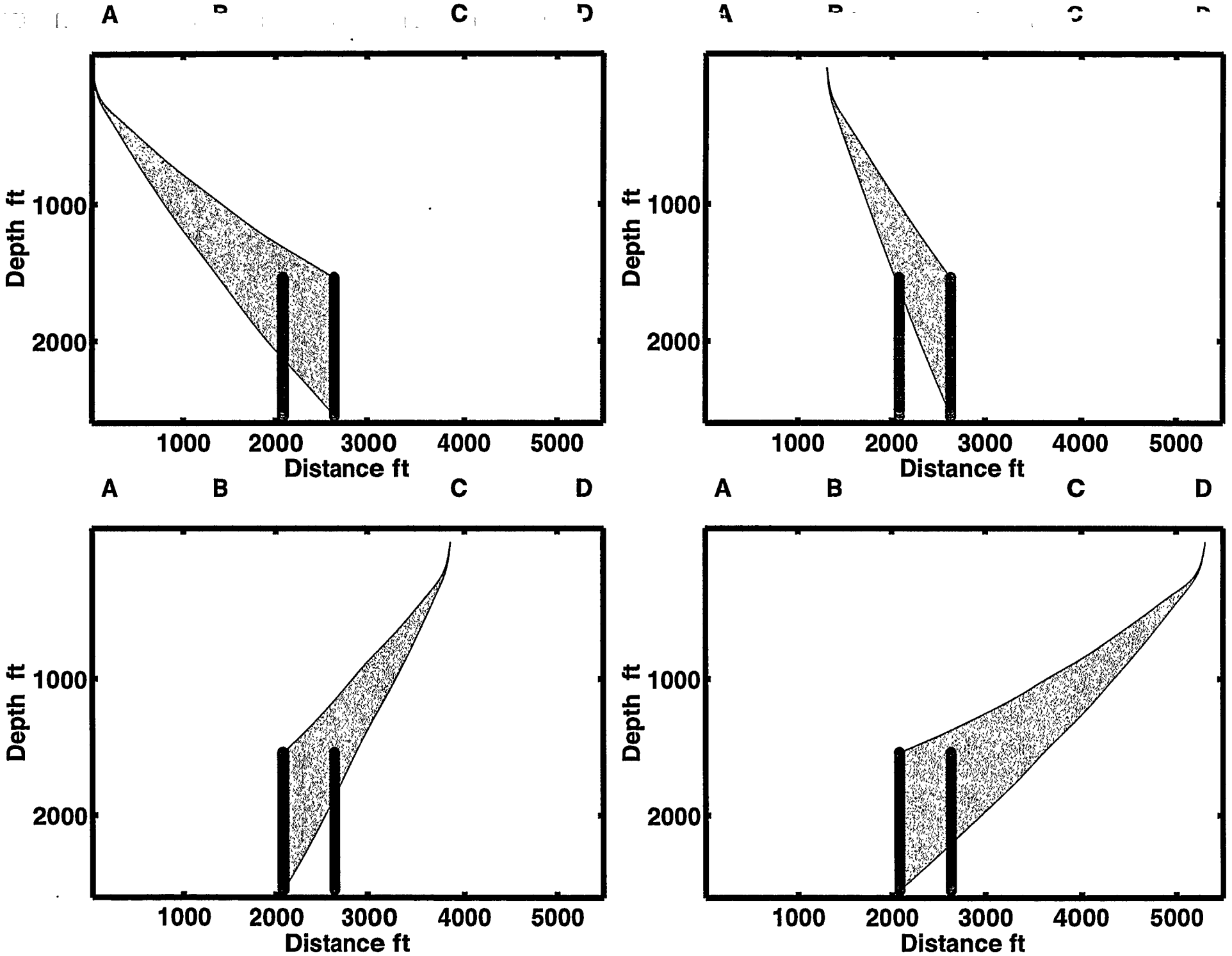

Figure 14: Raypath coverage from source location to far receiver well. Valid raypaths for the interwell tomography are those that intersect both receiver wells.

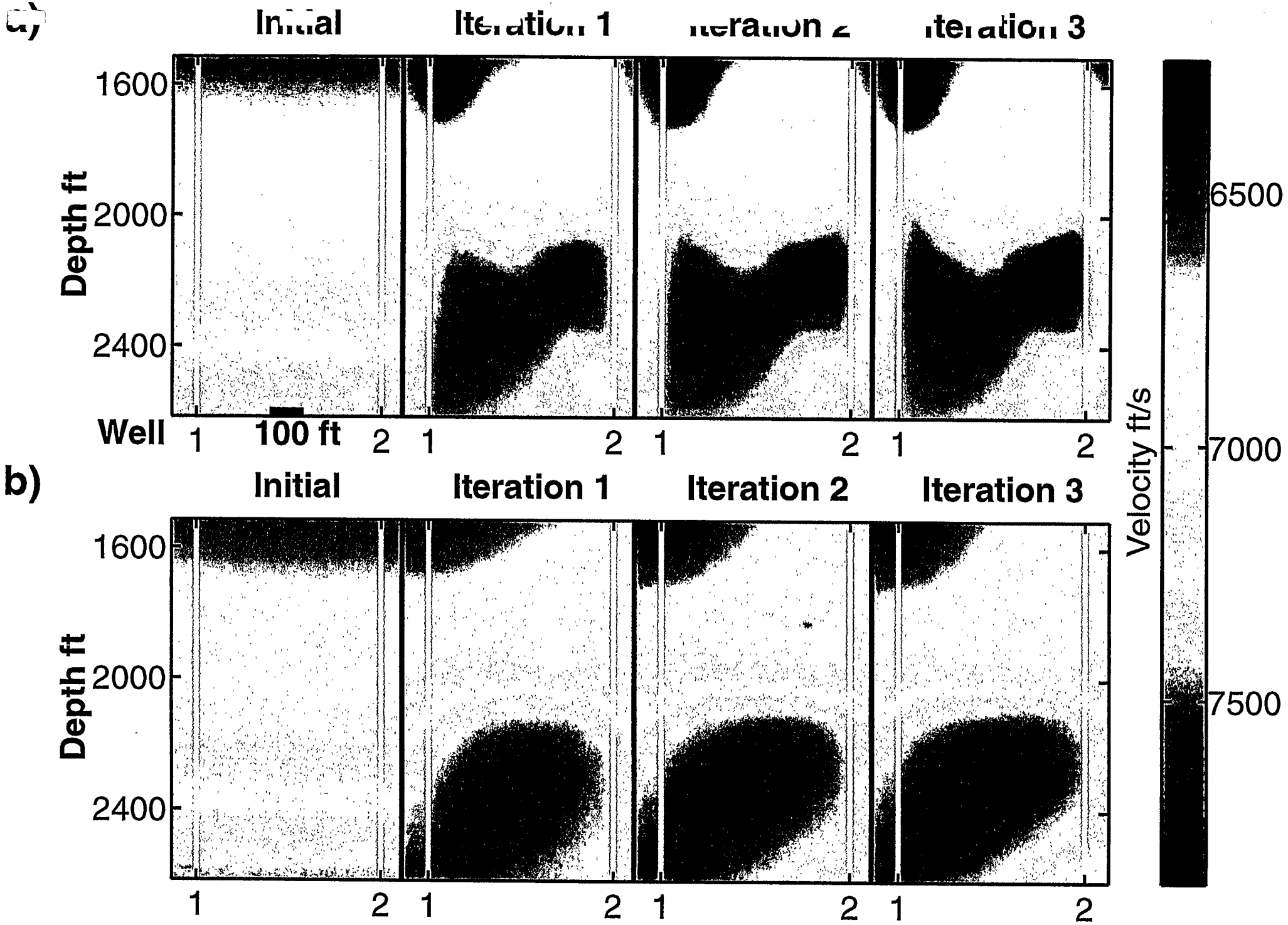

Figure 15: Estimated velocity models for the interwell inversion. a) Results assuming a low noise level in the first arrival times. b) Results assuming a high noise level in the first arrival times.

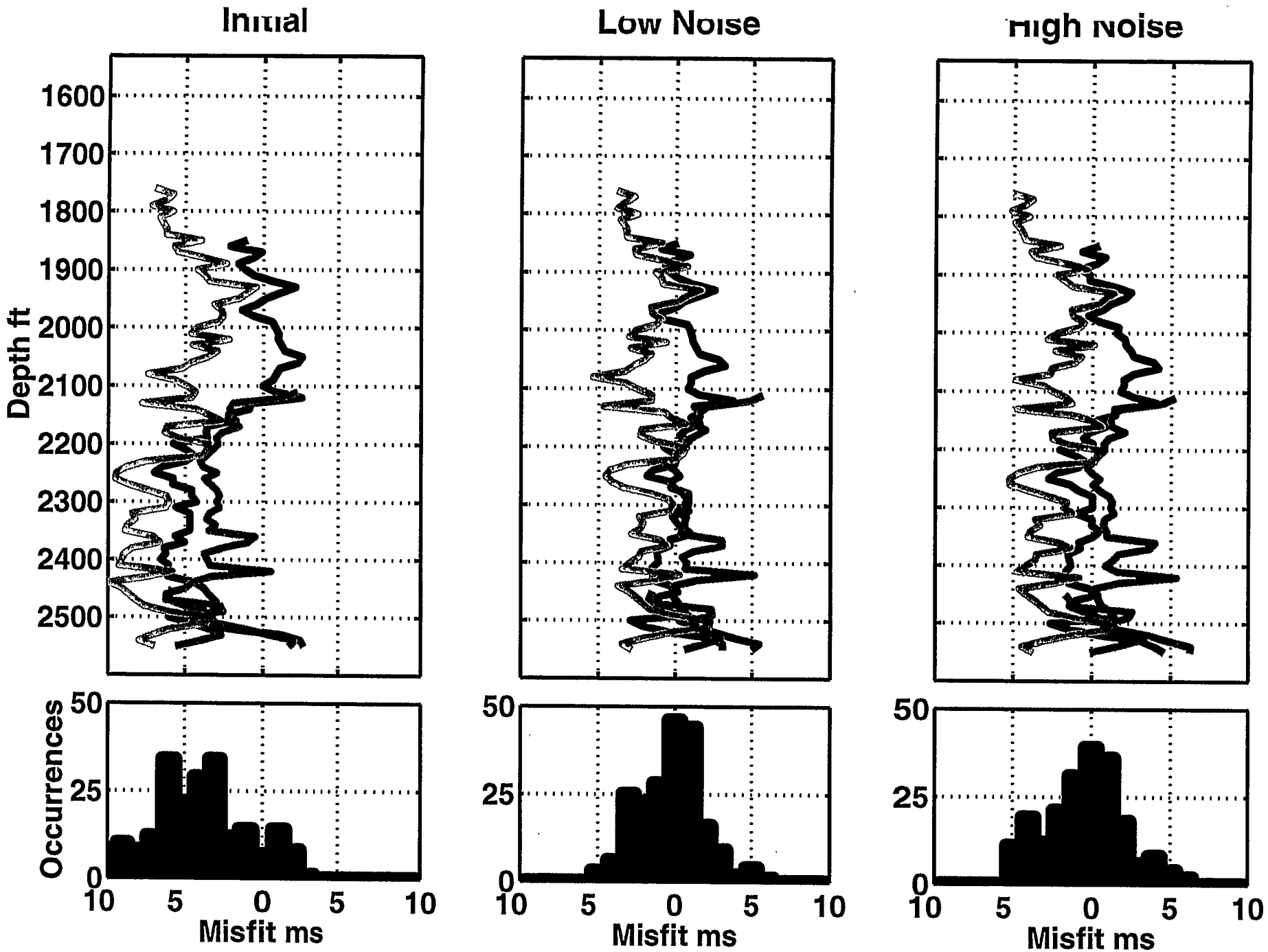

Figure 16: Data misfit for the interwell inversion. The initial data misfit, and the final data misfit after three iterations is shown as a function of receiver depth for the low noise and high noise examples. The color coding identifies the particular surface source location and shows the valid range of depths as implied by Figure 14. Histograms of the data misfit are also shown.

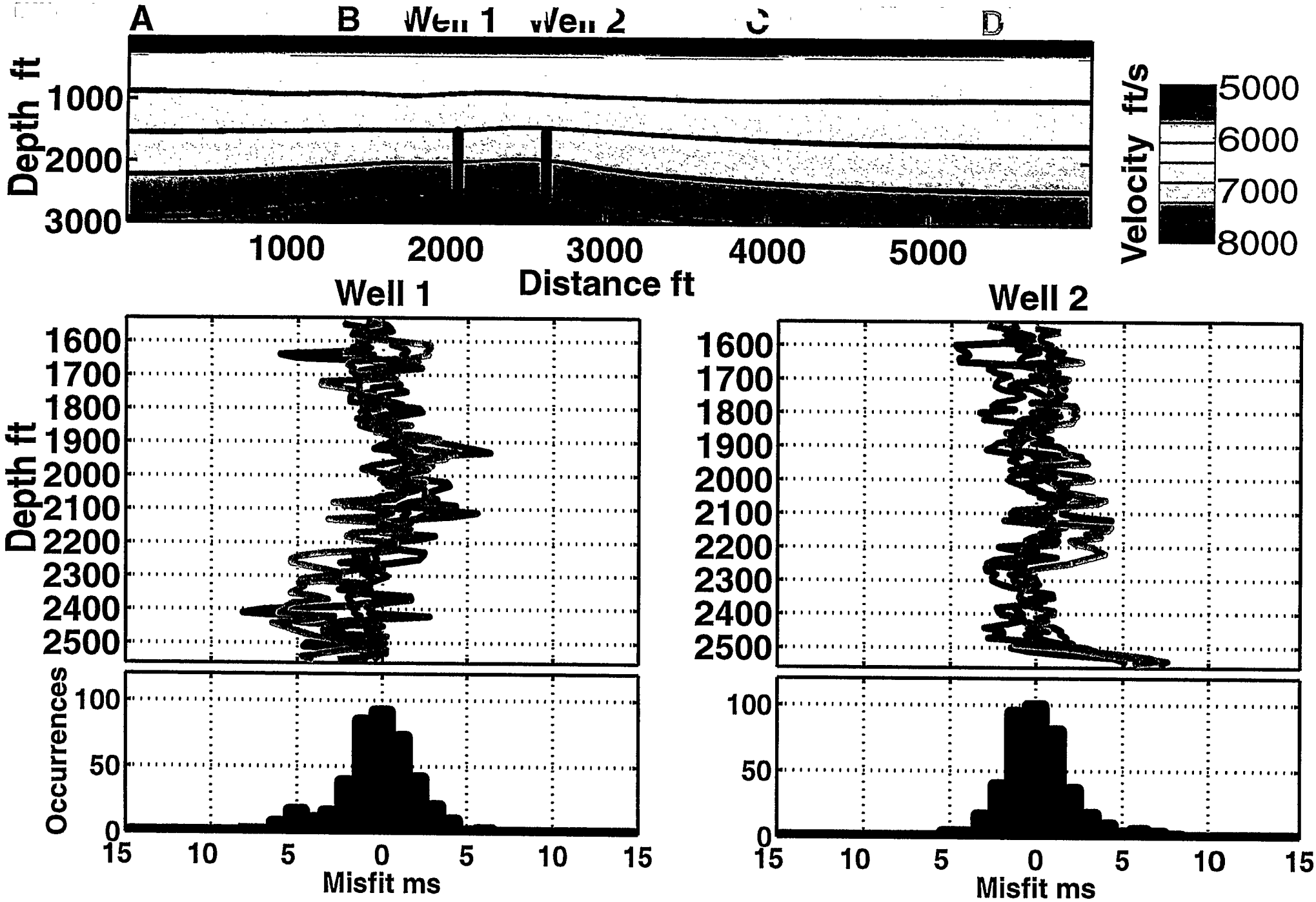

Figure 17: Final velocity model and data misfit for the surface source tomography.

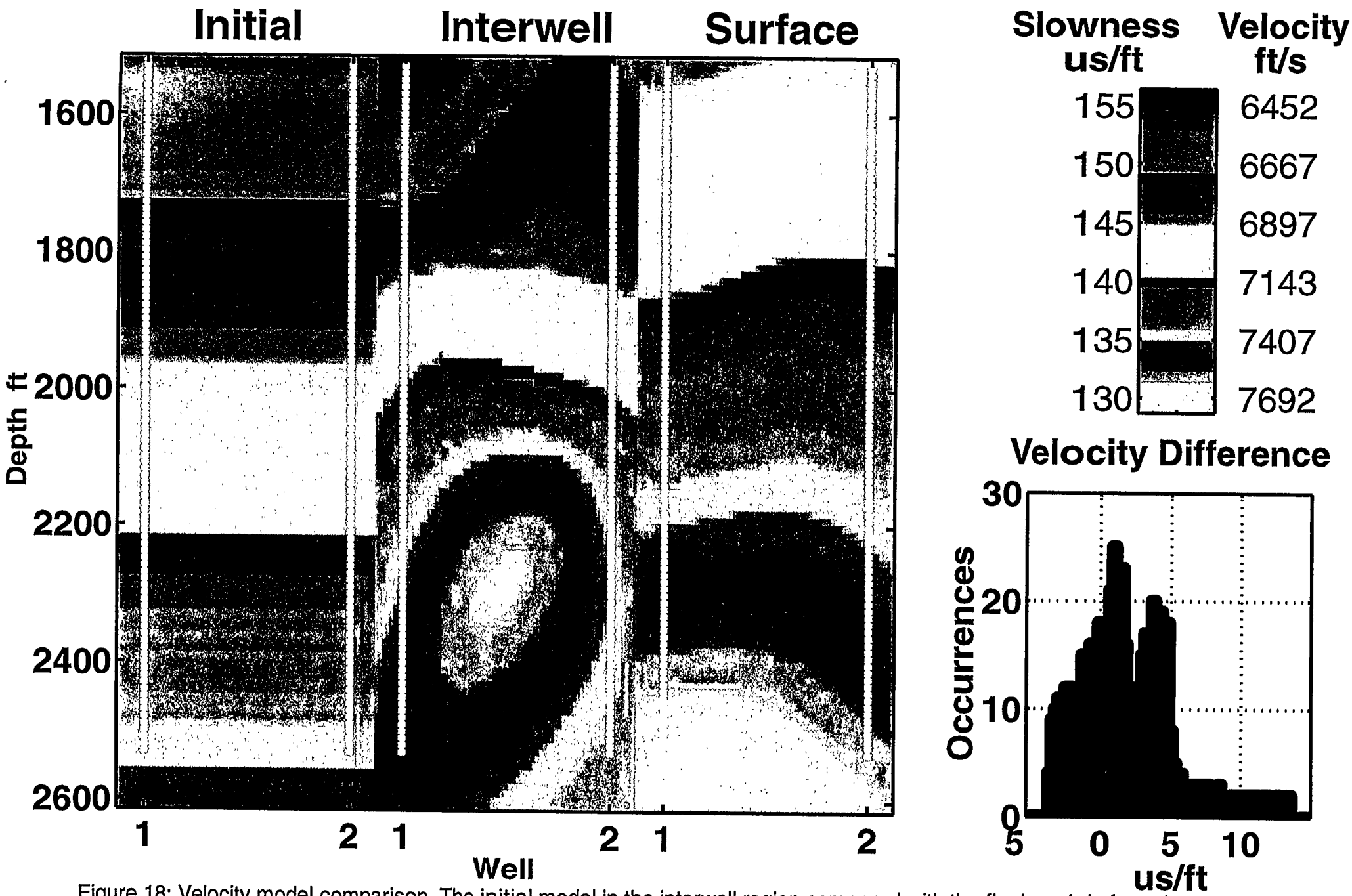

Figure 18: Velocity model comparison. The initial model in the interwell region compared with the final models from the interwell and surface source inversions. The histogram shows the difference between the final models from the interwell and surface source inversions.

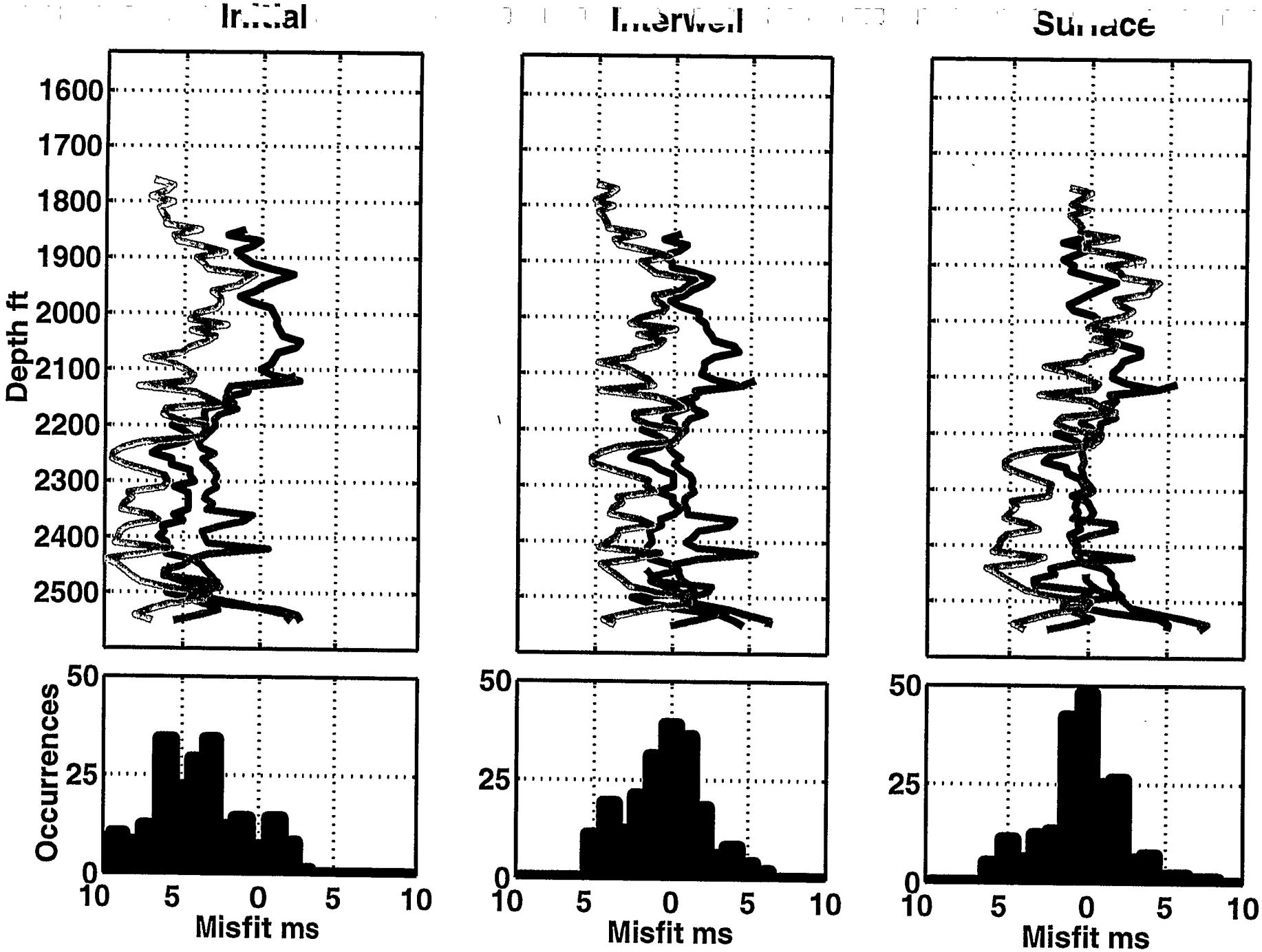

Figure 19: Initial data misfit compared with the final data misfit after the interwell and surface source inversions. The data misfit includes only those depths which are valid for the interwell inversion. Color coding indicates the respective surface source location•.